ABSTRACT

ESTIMATING OPTICAL PROPERTIES OF LIQUID PHANTOMS WITH MULTIPLE CORRECTION METHODS USING MEASUREMENTS FROM A SINGLE INTEGRATING SPHERE AND THE INVERSE ADDING-DOUBLE ALGORITHM

by Vinoin Devpaul Vincely

Integrating spheres (IS) are regarded as the gold-standard method to measure total reflectance and transmittance. These measurements combined with the high-speed solver, the inverse adding-doubling (IAD) method, provide efficient estimations of optical properties (absorption and reduced scattering) from thin unknown turbid samples. In this thesis, the performance of a table-top IS/IAD method to calculate optical properties will be explored using a robust set of optical phantoms whose properties mimic typical biological tissues. An analysis of the limitations of the system revealed light losses in IS measurements that translate to errors in inverse calculations. A robust Monte-Carlo model mimicking light propagation under the experimental configuration, is developed with simulations indicating relative errors in measurements up to 25%. Two commonly used correction methodologies, an experimental (substitution) and a theoretical (IAD-MC) correction protocol, were implemented to improve system performance. The effectiveness of these correction methodologies for multiple source configurations over a range of optical properties typical to biological media, was explored. These studies indicated that the theoretical correction along with a well collimated illumination source provide most accurate estimations of absorption and reduced scattering values by the IS/IAD method to within $0.05\,cm^{-1}$ and $0.8\,cm^{-1}$, respectively.

ESTIMATING OPTICAL PROPERTIES OF LIQUID PHANTOMS WITH MULTIPLE CORRECTION METHODS USING MEASUREMENTS FROM A SINGLE INTEGRATING SPHERE AND THE INVERSE ADDING-DOUBLE ALGORITHM

A Thesis

Submitted to the

Faculty of Miami University

in partial fulfillment of

the requirements for the degree of

Master of Science

Department of Physics

by

Vinoin Devpaul Vincely

Miami University

Oxford, Ohio

2020

Advisor: Karthik Vishwanath, PhD

Reader: Samir Bali, PhD

Reader: Imran Mirza, PhD

This Thesis titled

ESTIMATING OPTICAL PROPERTIES OF LIQUID PHANTOMS WITH MULTIPLE CORRECTION METHODS USING MEASUREMENTS FROM A SINGLE INTEGRATING SPHERE AND THE INVERSE ADDING-DOUBLE ALGORITHM

by

Vinoin Devpaul Vincely

has been approved for publication by

The College of Arts and Science

and

The Department of Physics

Karthik Vishwanath

Samir Bali

Imran Mirza

Table of Contents

List of Figures

List of Tables

Dedication

I dedicate this thesis to my loving grandmother, Regina, for her unending care, love and kindness. Her loss during the course of these studies has tremendously shaped me into the person I am today. Second, I want to than my parents, Vincely and Hema, for continually supporting me, emotionally, spiritually and financially. And lastly, I would like to thank the Almighty God, for the wisdom, guidance and the strength of mind for bringing this thesis to completion.

Acknowledgements

I would like to express a profound gratitude to my advisor, Dr. Karthik Vishwanath, for providing the guidance and perspective needed to be a successful researcher. His encouragement to ensure confidence in the details have been vital to the completion of this thesis. I would like to thank him for his patient mentorship that has helped me become a competent researcher through both my graduate and undergraduate years at Miami University. Next, I would like to thank my committee, Drs. Samir Bali and Imran Mirza for taking the time to read my thesis and offer helpful insights. I appreciate the great conversations, friendly banters and overall guidance in graduate school applications. Also the games of cricket, volleyball and badminton held as a department were some of my most fond memories in Oxford. Finally, I would like to thank each and every faculty and staff from the Department of Physics, whose constant encouragement and support have been instrumental in helping me complete this thesis and successfully finishing this graduate program.

Chapter 1

Introduction and Background

The goal of this thesis is to build a truly gold standard method of extracting broadband optical properties from thin unknown turbid samples. Literature holds the integrating sphere (IS) combined with the inverse adding-doubling (IAD) algorithm to be the most accurate and fast method of estimating sample optical properties. However, practical implementation of this method revealed high deviations in the estimations of optical properties from expected values. Two questions rose in the pursuit of answering these observations - ”Does the IAD predict sample optical properties accurately?” and ”Are the IS measurements given to the IAD accurate?”. The answers to these questions depend on various parameters such as sample optical properties, sphere and sample geometry, source profiles and detector efficiency.

The following chapter begins within an introduction to the typical nomenclature used in the field, the motivation and summary of the objectives of this thesis. In chapter 2, a detailed description of the IS/IAD method followed by a discussion of preliminary tests conducted using this method, is provided. In the pursuit of explaining observations seen in the preliminary analyses, Chapter 3 describes an ”in-house” developed Monte-Carlo method to simulate light propagation under given experimental conditions. Chapter 4 discusses prevalent issues observed with the IS/IAD method and ways to eliminate or mediate these effects in estimation of optical properties. Finally, chapter 5 concludes this thesis with a discussion of findings and possible avenues of future investigation.

1.1 Motivation

With advancements in laser technology, optical characterization of materials has become common place to investigate structure and composition of materials. Light-media interactions are studied using spectroscopic tools, that help quantify light absorbed, emitted, or fluoresced by any illuminated media. Turbid media, such as biological tissues, are a class of materials that purely absorb or scatter incident light. Understanding the distribution of light in biological tissues have allowed for the development of photochemical, thermal, and ablative modes of laser treatment protocols.

Wavelength-depended optical properties help quantify light distribution in turbid media. The optical properties of a sample govern the likelihood of an incident photon to either be absorbed or scattered. The optical absorption coefficient is defined as the inverse mean-free path a photon travels before being absorbed by the sample. Conversely, the optical scattering coefficient is defined as the inverse mean-free path between successive scattering events within a medium [1–3]. The light distribution through any homogeneous unknown media can be theoretically modeled given the optical properties of the media are known, hence operating in a forward fashion [1, 4–6]. These theoretical models are solutions to the equation of radiative transfer for specific sample and system conditions [4, 7].

Inverse models can estimate optical properties of unknown media, given that their light distribution can be accurately measured. Popular inverse methods function by iteratively running forward models to match measured light distributions with theoretical calculation [1, 7–9]. Models such as the inverse monte-carlo model, though accurate, prove to be computationally intensive for multi-wavelength analyses and at times inflexible to incorporate mismatched boundary conditions [5]. The inverse adding-doubling algorithm provides a practical method for high-speed estimation of sample optical properties at multiple wavelengths simultaneously [7, 10]. This combined with the integrating sphere to measure the total reflected and transmitted fluences provide an efficient method of estimating sample optical properties at wide wavelength ranges simultaneously [8, 10].

1.2 Nomenclature and Definitions

The fundamental nomenclature used in this thesis are presented here. First, a description of dimensional quantities, such as optical properties and fluence that describe light propagation in turbid media, are presented. This is followed by a discussion of dimensionless quantities such as albedo, optical depth, and anisotropy.

1.2.1 Dimensional quantities

We assume tissues to be turbid media that have a random distribution of localized spheres that either scatter or absorb photons. The advantage to this approach is that for perfect spheres the phase function is known [11] (see section 1.3.1). By this definition, the volumetric absorption and scattering coefficients can be defined as the inverse average distance between adjacent absorbing

and scattering centers respectively (table 1.1). The propagation of light through a sample modeled as a slab of finite thickness (d), can be described by the absorption and scattering coefficients and the phase function. The phase function refers to the fraction of light scattered from an incident direction ($\hat{s}$) to a scattered direction ($\hat{s}'$). The phase function is discussed in detail in section 1.3.1.

The net flow of photon energy, for a monochromatic source, is described by the radiance as a function of position and solid angle ($L(\vec{r},\hat{s})$). By integrating the radiance over all solid angles, the amount of energy deposited in a unit volume of the tissue can be obtained. This is referred to as the fluence ($\phi(\vec{r})$). The above mentioned dimensional quantities are summarized in table 1.1.

Quantity	Definition	Units
μ_a	Inverse of mean distance travelled by photon before absorption by sample	cm^{-1}
μ_s	Inverse of mean distance travelled by photon between successive scattering within sample	cm^{-1}
d	Thickness of sample	cm
$L(\vec{r},\hat{s})$	Radiance	$Wsr^{-1}cm^{-2}$
$\phi(\vec{r})$	Fluence (total radiance at point $\vec{r}$)	Wcm^{-2}

Table 1.1: List of dimensional quantities that describe light propagation in turbid media.

1.2.2 Dimensionless quantities

The dimensionless quantities commonly used in understanding light-media interactions are, the albedo, the optical depth (also known as optical thickness) and optical anisotropy of the sample. The albedo is defined as the ratio of scattering to the total attenuation ($\mu_a+\mu_s$) of the sample while the optical depth is defined as the product of sample thickness to the total attenuation. Finally, the optical anisotropy of the sample is the mean cosine of the angle (θ) of scattering by light from an incoming direction [10]. These quantities are summarized in table 1.2.

Quantity	Name	Expression	Typical Values
a	Albedo	$a=\frac{\mu_s}{\mu_a+\mu_s}$	$0-1$
b	Optical Depth	$b=d(\mu_a+\mu_s)$	$0-\infty$
g	Anisotropy	$g=<cos(\theta)>$	$-1-1$

Table 1.2: List of dimensionless quantities

1.3 Equation of Radative Transport

In this section, the transport equation that describes the behavior of light in a turbid slab, is explored. The following is the fundamental form of the transport equation (1.1).

$$(\hat{s}\nabla)L(\vec{r},\hat{s}) = -\mu_t L(\vec{r},\hat{s}) + \mu_s \int_{4\pi} p(\hat{s},\hat{s}')L(\vec{r},\hat{s})d\Omega' \tag{1.1}$$

The above equation models the rate of change of intensity at a point $\vec{r}$ and in a direction $\hat{s}$ (L.H.S of equation 1.1). This rate of change is equal to the loss of intensity due to attenuation (in the form of scattering and absorption by media) plus a gain in intensity due to light scattered in the direction $\hat{s}$ from all other directions (last term on the R.H.S of equation 1.1). This indicates that the distribution of intensity is dependent on the position and direction.

The transport equation operates on key assumptions that are described below. Firstly, the medium modelled is assumed to be homogeneous, i.e. the length scales of variations in scattering and absorption of the medium are much smaller than the sample thickness. Secondly, it is assumed that each scattering particle is sufficiently isolated that the overall scattering pattern is independent of all other particles. Thirdly, it is assumed that scattering by all particles may be described by a single function known as a phase function. This leads to the conclusion that there exists an ensemble average scattering pattern for all the scattering centers in the medium. Finally, an assumption that there are no light sources within the medium is also made.

1.3.1 Phase functions

The phase function describes the scattering profile of light incident on a particle with a refractive index different from the media it is enclosed in. The angle of refraction of the light incident on these particles, will depend on the wavelength of the light, the angle of incidence and the refractive index of the particle. The phase function (denoted as $p(\hat{s},\hat{s}')$) describes the amount of light scattered into the direction $\hat{s}'$ from an incident direction of $\hat{s}$. The phase function can be normalized across all possible angles of scattering,

$$\int_{4\pi} p(\hat{s},\hat{s}')d\Omega = 1 \tag{1.2}$$

where $d\Omega$ is a differential solid angle in the $\hat{s}$ direction. The phase function is a description of light scattering by the particle and does not permit absorption. For simplicity, the phase function is constrained as the mean phase function while also assuming the probability of scattering is purely a function of the angle between incident and scattered directions (i.e. $p(\hat{s},\hat{s}') = p(\hat{s}.\hat{s}') = p(cos\theta)$.

The simplest phase function will be the isotropic phase function, expressed as $p(\hat{s},\hat{s}') = \frac{1}{4\pi}$ where the factor, $1/4\pi$ is a result of the normalization condition and the fact that there are 4π steradians in a complete circle. However, for non isotropic phase functions, a parameter called the average cosine of the phase function is used to describe the degree of anisotropy of the phase function. This parameter is often denoted by g and is denoted as the integral over all angles of the phase function multiplied by the cosine of the angle

$$g = \int_{4\pi} p(\hat{s}.\hat{s}')(\hat{s}.\hat{s}')d\Omega \tag{1.3}$$

The choice of a single scattering phase function is a balance between realistic modelling and mathematical feasibility. The single particle light scattering in human tissues can be accurately modeled using the modified Henyey-Greenstein function [7, 12] (eq. 1.4).

$$p(cos\theta) = \frac{1}{4\pi}\left[\beta + (1-\beta)\frac{1-g^2}{(1+g^2-2gcos\theta)^{3/2}}\right] \tag{1.4}$$

where β describes the amount of light scattered isotropically and the fractional term is the Henyey-Greenstein function. The function can be normalized such that the integral over all solid angles is unity. The phase function reduces to the Henyey-Greenstein phase function when $\beta = 0$. The average cosine of the phase function g is a measure of how much light is scattered in the forward direction. The anisotropy can be any value between -1 and 1 where a value of g = -1 corresponds to scattering completely in the backwards direction. A value of g = 1 is when scattering is purely in the forwards direction and finally a value of g = 0, is isotropic scattering.

1.3.2 Adding-Doubling

A general numerical solution to the equation of radiative transfer is the Adding-Doubling (AD) method [7, 13]. The AD method is a high speed forward method to calculate light distribution across a sample with known optical properties. This is achieved by solving the RTE in one-dimension, while not violating the assumptions mentioned in section 1.3. This simplification of the RTE results in samples modelled as thin-infinite slab, i.e. a sample extending infinitely in directions normal to photon incidence while maintaining a finite thickness (fig. 1.1) [7, 13].

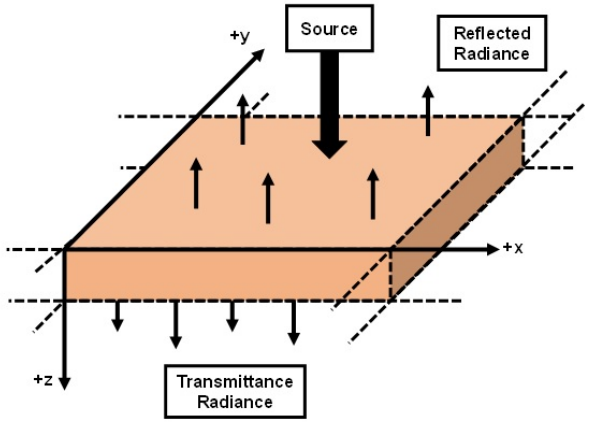

Figure 1.1: AD visualization of a homogeneous turbid sample with known optical properties.

The name ”adding-doubling” corresponds to estimation of total reflectance and transmittance for a slab of desired thickness and known optical properties. By juxtaposing identical slabs and summing the contributions from each slab the total reflectance and transmittance is found [13, 14]. This modelled can be adjusted to allow simulations of media with different layers with uniform optical properties and internal reflections at the boundaries of these layers [13]. A detailed description and the implementation of the AD method is described in section 3.2.

1.4 Thesis Objectives

The primary goal of this thesis is to estimate the total scattering and absorption of turbid liquid media, with high accuracy and precision under the most efficient experimental protocols. As mentioned in section 1.1, the IS/IAD method proves to be such a method capable of high-speed multi-wavelength estimation of optical properties. There are two main tasks to this thesis - 1) To test the IS/IAD method with liquid optical phantoms with wide range of optical properties, most similar to typical biological tissues. 2) The development of a robust Monte Carlo model for simulating light propagation through a sample mounted on an integrating sphere.

Chapter 2

Experimental Requirements

To estimate optical properties of unknown turbid samples, two fundamental measurements are to be made using the IS system - total reflectance and transmittance. These measurements, once made, are given as inputs to an appropriate inverse model, along with other sample and sphere parameters, that can then estimate broadband optical properties of the samples. The following is a schematic of the overall experimental protocol used in this thesis to estimate optical properties of turbid samples (fig. 2.1).

Figure 2.1: Typical workflow of the IS/IAD method to extract sample optical properties

The following sections will elaborate components of this workflow in greater detail. We begin with a detailed description of the integrating sphere and the theory behind light collection of this device. The chapter is then concluded with a brief introduction to inverse modelling and why it is vital for the estimation of optical properties.

2.1 Integrating Sphere

The integrating sphere (IS) is a well established technique of measuring the total reflected and transmitted fluence of thin samples [1, 7, 8, 10, 15]. The IS by design is a spherical device with its interior surface coated by a highly reflective material. Commercial IS devices use barium sulfate (Spectraflect) or a polymer of Teflon, polytetrafluoroethylene (PTFE) as its reflective coating. Across the

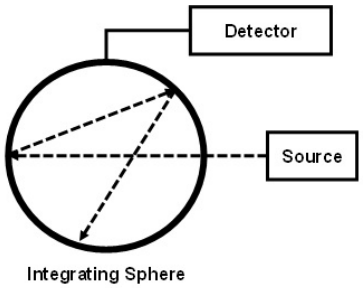

Figure 2.2: Illustration of a simple integrating sphere system.

spherical body of the device, finite sized ports are positioned so as to allow the mounting of a sample, a detector or light to illuminate the device (as seen in 2.2).

The total reflected (R_t) and transmitted (T_t) fluence of a thin sample can be measured by uniquely orienting the sample with respect to the sphere and source. By placing the sample on a port that is on the farther side of the sphere, all light reflected off the sample can be collected. Conversely, by placing the sample on a port in between the sphere and the source, all transmitted light is collected. These orientations are visually described in figure 2.3.

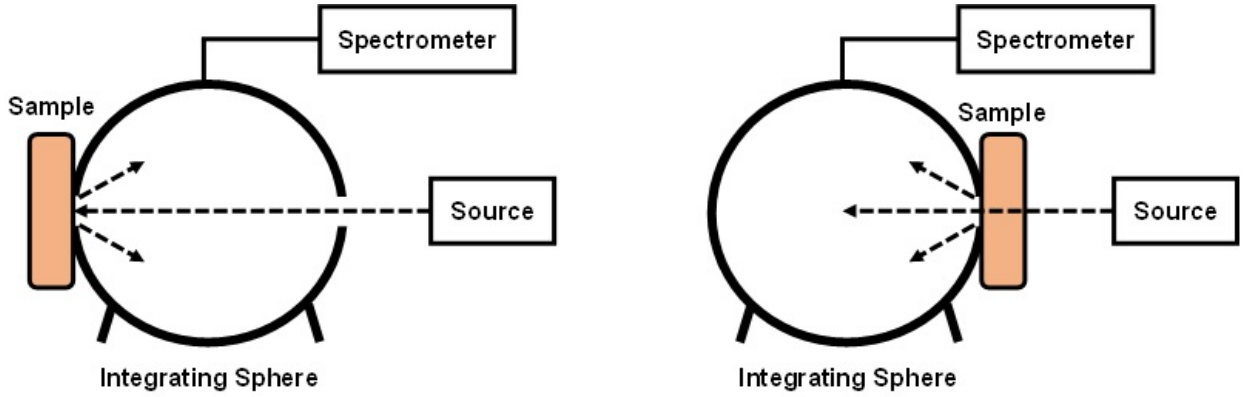

Figure 2.3: Integrating sphere orientations for reflectance (left) and transmittance (right) measurements.

The total reflectance (R_T) and transmittance (T_T) are normalized expressions of intensity signals measured using a commercial spectrometer mounted onto the sphere (as described in fig. 2.3) (eq. 2.1). For the reflectance measurement, R_{dark} refers to baseline signal collected by the system when the sphere is not illuminated, i.e. source is turned off. $R_{standard}$ refers to a signal measured when the a 100 % reflective calibration standard mounted onto the IS sample port, is illuminated by the source. The R_{sample} refers to the signal measured when a sample is mounted onto the IS sample port. Conversely, in the measurements of total transmittance, T_{dark} refers to a similar baseline signal collected by the system when the sphere is not illuminated. T_{empty} corresponds to the signals measured when sample port is empty in the transmittance configuration and the source allowed to illuminate the sphere. Finally, T_{sample} refers to the signal measured when a sample is mounted onto the IS sample port. This process ensures, that the measured reflectance and transmittance straddles between $0 - 100$ % for any given sample.

$$R_T = \frac{R_{sample} - R_{dark}}{R_{standard} - R_{dark}} \qquad T_T = \frac{T_{sample} - T_{dark}}{T_{empty} - T_{dark}} \tag{2.1}$$

For the following studies, a 6-inch diameter IS with an internal coating of Spectraflect is used (*Labsphere RT-060-SF)*. Five 1-inch ports and one 0.5-inch port populate the surface of the device. The 1-inch ports are purposed for either mounting a sample or allowing an illumination beam while the 0.5-inch port is used to mount a detector. Finally, a baffle, a small reflective shield, is positioned such that light specularly reflecting off the sample is redirected away from the detector.

Depending on the application various combinations of sources and detectors can be coupled with the IS systems. For the studies conducted in this thesis, two types of illumination sources will be used - a broadband continuous-wave halogen source (*Thorlabs Inc. SLS202L*) and a pulsed supercontinuum source (*NKT Photonics SuperK EVO ERL-04*). Varying optics populate the path depending on the type of source used for sample illumination. The halogen source produces a highly diverging Gaussian beam profile. Due to this divergence, a in-house built collimator (using a set of converging and diverging lens) is used to ensure beam collimation. The best collimation ensured is a spot size of 17 mm diameters. The bandwidth of the pulsed supercontinuum source is controlled using a bandpass filter (*NKT Photonics SuperK VARIA*). Due to the pulsed characteristic of this source, a well collimated beam (1.5 mm diameters) is guided using a set of mirrors to illuminate the sample.

With a goal of obtaining optical properties of highly turbid media over visible wavelength ranges, a UV-VIS spectrometer operating with high signal-to-noise ratios is need. Here, *StellarNet SILVER-Nova*, a cooled spectrometer for low light applications is used in conjuncture with both halogen and superconntiunm sources.

2.1.1 Theory of Integrating Sphere

The total counts measured by a standard detector mounted onto an integrating sphere, is depended on the total power incident upon the detector and the response to that power. However, interactions between the sample and sphere affects the detected signal in such a way that it is no longer proportional to the true reflectance or transmittance of a sample [10, 16–18]. To better understand this, let us consider a sphere with an internal radius of R and other parameters listed in table 2.1. It is assumed that the reflectivity of the sphere wall (m) is invariant of wavelength.

Parameter	Expression
Total area of sphere wall	$A = 4\pi R^2$
Reflectivity of sphere wall	m
Area of detector port	δ
Area of sample port	s
Total area of other ports	h
Relative area of sphere wall	$\alpha = 1-(\delta/A+s/A+h/A)$

Table 2.1: A list of integrating sphere parameters

First, consider a situation where all ports on the sphere, except one, are closed using a similar material as the interior coating of the sphere. The one port that remain open is used to allow a well collimated beam (with power P) to illuminate the sphere. The total power collected by the detector for the first reflection can then be expressed as,

$$\frac{\delta}{A}mP \tag{2.2}$$

After the first reflection, a fraction of the power incident on the detector can interact with a mounted sample, be lost through any open ports (if any) or undergo a second reflection by the sphere walls. Hence, the total power collected by the detector for a second reflection can be expressed as,

$$\frac{\delta}{A}mP + m\alpha mP + R_d\frac{s}{A}mP = mPF, \tag{2.3}$$

where.

$$F = \frac{\delta}{A} + m\alpha + R_d\frac{s}{A} \tag{2.4}$$

Equation 2.4 represents the fraction of the total incident light that is diffusely reflected by all the components of the IS. The factor R_d represents the reflection coefficient of the sample illuminated diffusely, resulting in a loss in power detected. For each subsequent reflection, the power collected by the detector incurs a loss as a factor of F and hence the total power collected by the detector for

the n^{th} reflection is given by,

$$P_d = \frac{\delta}{A} mP(1 + F + F^2 + ... + F^{n-1}) \tag{2.5}$$

This response of the integrating sphere can be experimentally probed using well-calibrated reflectance standards. To understand this for our integrating sphere, a set of four reflectance standards - $2\%, 50\%, 75\%$ & 99% (*Labsphere RSS-04-020*), that have flat spectral profiles across wide wavelength ranges, were used. Figure 2.4 describes the discrepancies in the IS measurements against manufacturer calibration specified values. It can be observed that the highest deviations in measured total reflectance values can be observed for samples that are 50% reflecting. Hence, typical reflectance measurements of biological tissues can experience relative errors up to 15%.

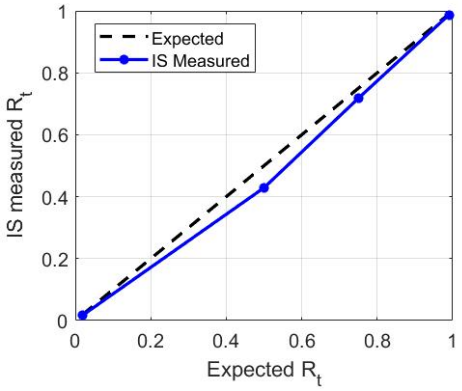

Figure 2.4: Relationship between IS measured values and true values of various calibration standards at 500 nm.

2.2 Inverse Modelling

Conventional methods of estimating sample optical properties involves the use of solutions to the equation of radiative transfer (as mentioned in section 1.3), that express optical properties in terms of measured parameters [7]. However, in practice, the optical properties can only be obtained by solving the "inverse problem". This problem refers to the constrained ability to place optical properties in a light propagation model and have the corresponding values of total reflectance and transmittance be computed. Over iterations, these optical properties are adjusted until computed reflectance and transmittance match measured values within certain tolerances [1, 15, 19].

As mentioned in section 2.1, the integrating sphere can be used to make measurements of total reflectance and transmittance on thin turbid tissues. The relationship between measurements and the optical properties have been explored in two ways - analytical models (such as multiple-flux models, diffusion theory and adding-doubling method) and Monte-Carlo modelling [1, 15, 19]. While

Monte-Carlo models provide robustness in modelling specific source-tissue-detector geometries, they are constrained by long computational times due to their stochastic nature (see chapter 5). On the other hand, analytic models are more elegant as they provide closed form expressions of R_t and T_t in terms of the sample optical properties.

The number of measurements made on a given sample is directly proportional to the number of optical properties a given inverse model can estimate, i.e. if only measurements of R_t and T_t are made, then it is not possible to estimate all three optical properties (μ_a, μ_s & g). However, if it is assumed that for a slab with optical properties, μ_a, μ_s & $g \neq 0$ have similar R_t and T_t to another slab with optical properties, μ_a, μ_s & $g = 0$, two independent quantities (μ_a and μ_s') can be estimated (where $\mu_s' = \mu_s(1-g)$). This approximation, known as the "Similarity Principle" holds true only for tissue models of finite thickness and breaks down for models with thickness' comparable to the effective penetration depth ($1/\mu_t$).

Due to the closed form expressions of analytical models, solutions can be computed with high efficiency. However, this efficiency comes at a cost to the overall accuracy of the model in comparison to more accurate Monte-Carlo models. Hence, the optimum choice for a model to derive optical properties from any given measurement involves a trade-off between accuracy, speed and the ability to fully describe the experimental arrangement. As described in section 1.3.2, the AD is a high speed solution to the 1D-RTE and can be used to solve the inverse problem efficiently. In the following chapter, this inverse model, the Inverse Adding-Doubling will be explored in great detail.

Chapter 3

Inverse Adding Doubling Method

The inverse adding-doubling (IAD), is an inverse iterative method of translating measured sample parameter (total reflectance and transmittance) to optical properties. As described in section 2.2, this model makes uses of the 1-D forward adding doubling algorithm [7, 16, 20–22], which allows high speed estimation of optical properties compared to more rigorous methods, like the inverse monte-carlo method [15, 23, 24]. The following aspects comprise the iteration process of the IAD (fig. 3.1),

- An initial guess of optical properties under given constraints.
- AD estimates total reflectance and transmittance values for guessed optical properties.
- The error between AD estimations and measured values is calculated.
- The process is repeated until error is within a desired tolerance.

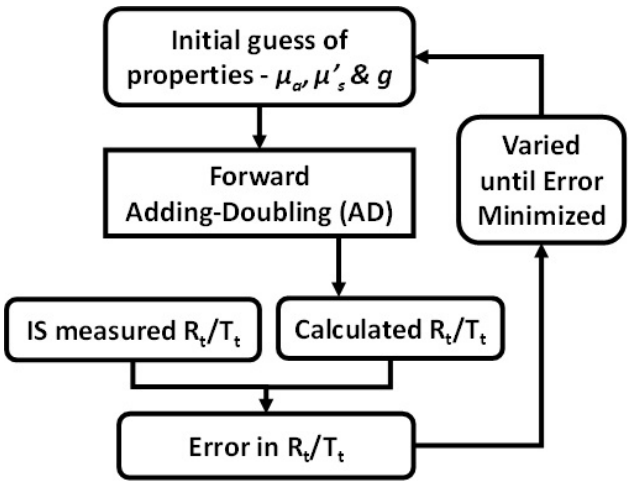

Figure 3.1: A schematic describing the basic workflow of the IAD in estimating optical properties from a set of experimental measurements.

In the following sections, the various routines of the IAD in estimating optical properties from a set of integrating sphere measurements, will be explored in greater detail.

3.1 Initialization of Inverse Calculations

The iteration method implicitly assumes that a given set of reflection (R_t), transmission (T_t) and unscattered transmission (T_c) measurements can determine a unique combination of sample albedo, optical depth and anisotropy. However, for thicker samples, an accurate measurements of unscattered transmittance may no be possible. Hence, the IAD is designed under two unique cases - fixed unscattered transmission and fixed scattering anisotropy. The former is representative of when three measurements (R_t, T_t, T_c) can be made on a given sample and allowing the estimation of all three optical properties (μ_a, μ_s, g). The latter applies when the unscattered transmission measurement is unavailable for the sample, allowing only two measurements (R_t, T_t) to be made resulting in the estimation of two optical properties (μ_a, μ_s'). For the studies in this thesis, only two measurements are made on all samples. In this case, a value for the scattering anisotropy is assumed, and the albedo and optical thickness are calculated based on this assumed value.

The initial guess of the optical properties affects both the rapidity and accuracy of the convergence. Poor initial guess leads the minimization algorithm to converge into a local minima than the global minimum. Generating an appropriate set of initial values of optical properties for a combination of R_t and T_t is difficult. Using the similarity relations described by *van de Hulst*, one can facilitate the initial guessing of optical properties (a, b, g) by relating them to a set of reduced optical properties (a', b', $g = 0$) [14].

$$a = \frac{a'}{1-g+a'g} \qquad\qquad b = b' + \frac{a'b'g}{1-g} \tag{3.1}$$

This reduces the iteration process to finding two parameters (a', b') from a set of two measurements (R_t, T_t). A good starting guess of the reduced albedo and reduced optical thickness is based on a crude fit of the reflection and transmission values,

$$a' = \begin{cases} 1 - \left(\dfrac{1-4R_d-T_t}{1-T_t}\right)^2 & \text{if} \quad \dfrac{R_d}{1-T_t} < 0.1 \\ 1 - \dfrac{4}{9}\left(\dfrac{1-R_d-T_t}{1-T_t}\right)^2 & \text{if} \quad \dfrac{R_d}{1-T_t} \geq 0.1 \end{cases} \tag{3.2}$$

$$b' = \begin{cases} \dfrac{-\ln T_t \ln(0.05)}{\ln R_t} & \text{if} \quad R_d \leq 0.1 \\ 2^{1+5(R_d+T_t)} & \text{if} \quad R_d > 0.1 \end{cases} \tag{3.3}$$

By using equations 3.1, 3.2 and 3.3, initial values of the albedo and optical thickness can be generated and proceed with the inverse processes of the IAD.

3.2 Adding-Doubling Method

In this section the adding-doubling (AD) method for solving the equation of radiative transport method, is described. The key advantages of the AD method are that only integration over angles are required, physical interpretations of the results can be made an any iteration of the model, both isotropic and anisotropic scattering can be handled, and results can be obtained for all angles of incidence used in the integration. The AD method is well suited for iterative problems as it provides accurate estimates of total reflectance and transmittance with relatively few quadrature points (see below). The following assumptions are made for all calculations done using this method,

- The distribution of light is invariant of time.
- Light is unporlarized and azimuthally symmetrical.
- The sample is a slab of homogeneous optical properties.
- The sample has a uniform index of refraction.
- At boundaries, the internal reflection is governed by Fresnel's law.
- The ambient medium is non-absorbing with a different refractive index.

The AD calculates reflection ($R(\theta,\theta')$) and transmission ($T(\theta,\theta')$) for light incident at angle θ and exciting at an angle θ' through a slab of desired thickness and known optical properties. The model begins by modelling a sufficiently thin slab, for which reflection and transmission can be accurately calculated using the single scattering approximations. With knowledge of the transmission and reflection for this arbitrary slab, the "doubling" method then determines the reflection and transmission of a slab twice as thick by juxtaposing two identical slabs and summing the contributions of the individual layers to the overall reflection and transmission of both slabs. The "adding" method extends the doubling method to slabs with varying optical properties. Thus, by placing these dissimilar slab adjacent to one another, light propagation through layered media can be simulated.

3.2.1 Nomenclature

Due to the azimuthal symmetry of the model, the samples reflection and transmission are tagged with the angle made with the normal by any entering ($v = \cos(\theta)$) or exiting ($v' = \cos(\theta')$) radiance. Hence, the incident radiance can be denoted as $L^{+}_{incident}(v)$, where $+$ indicates the direction of propagation ($+z$ direction, downwards) (Fig. 3.2). For the modelled tissue, the reflection and transmission function, $R(v',v)$ and $T(v',v)$ respectively, are defined in the propagating direction v' from the incident direction v [14]. With these definitions, the total transmitted and reflected radiance by a modelled sample can be written as,

$$\begin{aligned} L^{+}_{transmitted}(v') &= \int_0^1 L^{+}_{incident}(v)T(v',v)2vdv \\ L^{-}_{reflected}(v') &= \int_0^1 L^{+}_{incident}(v)R(v',v)2vdv \end{aligned} \tag{3.4}$$

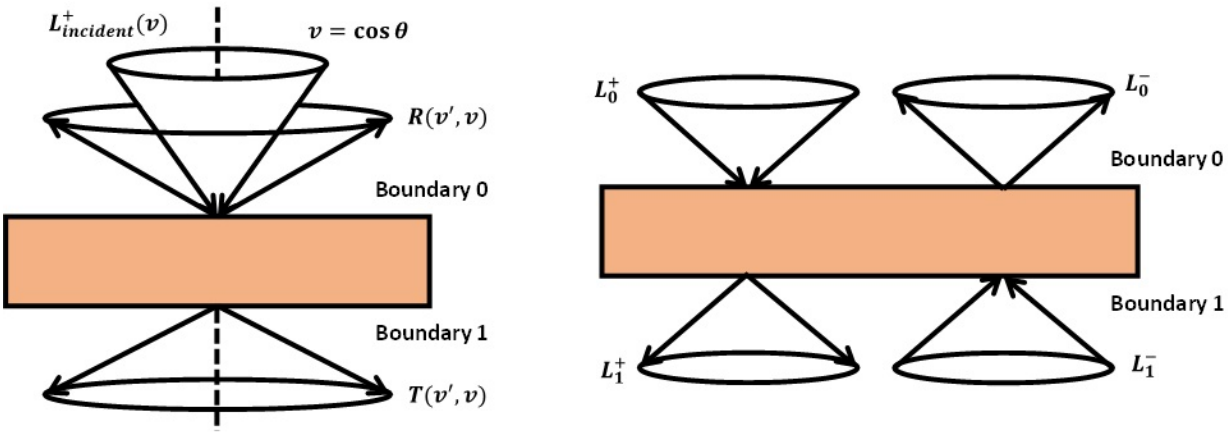

Figure 3.2: Schematic representation of the nomenclature used by the AD to estimate reflectance and transmittance through a sample of known optical properties (Left). Nomenclature for the upward and downward radiances from each surface of an arbitrarily defined slab (Right).

3.2.2 Quadrature Scheme

In order to perform the integrations described in equations 3.4, an appropriate quadrature scheme will be used to approximate these integrals. As an example, the integration of a function $f(x)$ over the integral (a,b) with a weighting function $g(x)$ using M points can be approximated as follows,

$$\int_a^b f(x)g(x)dx \approx \sum_{i=1}^{M} f(x_i)w_i \tag{3.5}$$

here, the integration points x_i and weights w_i are chosen in such a way that the integration will integrate a polynomial of degree $2M$ exactly. The extension to two arbitrary functions can be expressed as,

$$\int_0^1 A(x,x')B(x,x')2x'dx \approx \sum_{j=1}^{M} \mathbf{A}_{ij} 2v_j w_j \mathbf{B}_{ik} \equiv \mathbf{A}\ \mathbf{B} \tag{3.6}$$

Equation 3.6 shows explicitly the relationship between integration and matrix multiplication, where they differ from factor of $2v_j w_j$ that must be included. This can be done by introducing a identity matrix $\mathbf{E}$ for matrix multiplication of this type,

$$\mathbf{E}_{ij} = \frac{1}{2v_i w_j}\delta_{ij} \tag{3.7}$$

here δ_{ij} is the Kronecker delta function. *Grant and Hunt* have shown that an algebra based on this implied multiplication is a semigroup, and have proven that all manipulations that follow are valid [25].

3.2.3 Matrix Relations for Adding Layers

According to *Plass et. al.*, the light incident on side 0 of an arbitrary slab, moving towards side 1 can be represented by a set of operators. These operators are the reflection and transmission operators represented as $R^{01} = R(v_0, v_1)$ and $T^{01} = T(v_0, v_1)$ respectively. For a homogeneous slab, $R^{01} = R^{10}$ and $T^{01} = T^{10}$ due to symmetry across both directions of propagation. Here, v_0 and v_1 are chosen corresponding to the quadrature scheme adopted. As described in figure 3.2 (right), the vector $L_0^+(v)$ refers to the radiance incident on side 0 of a arbitrarily thick slab, and $L_1^-(v)$ is the radiance incident on side 1. Similarly, $L_0^-(v)$ and $L_1^+(v)$ are defined as the radiance exiting the slab from sides 0 and 1 respectively. As described in section 3.2, the downward radiance exiting the slab from side 1 is the sum of the incident radiance transmitted from side 0 and reflected radiance from side 1,

$$L_1^+ = T^{01}L_0^+ + R^{10}L_1^- \tag{3.8}$$

Similarly, the upward radiance from side 0 is the sum total of the radiance transmitted from side 1 and the reflected radiance from side 0,

$$L_0^- = R^{01}L_0^+ + T^{10}L_1^- \tag{3.9}$$

Analogous formulas can be used to describe another arbitrary layer with boundaries 1 and 2 as follows,

$$\begin{aligned} L_2^+ &= T^{12}L_1^+ + R^{21}L_2^- \\ L_1^- &= R^{12}L_1^+ + T^{21}L_2^- \end{aligned} \tag{3.10}$$

As mentioned in section 3.2, the two layers 01 and 12 can be juxtaposed to yield a combined layers 02. The equations for the layers with sides 0 and 2 are,

$$\begin{aligned} L_2^+ &= T^{02}L_0^+ + R^{20}L_2^- \\ L_0^- &= R^{02}L_0^+ + T^{20}L_2^- \end{aligned} \tag{3.11}$$

Given the reflection and transmission operators for the layers 01 and 12 are known, similar operators for the layer 02 can be produced in terms of those for the individual layers 01 and 12. By left-multiplying R^{12} to the elements of equation 3.8 and adding them to the equation describing L_1^- (eqs. 3.10), allows one to solve for the upward radiance at the interface between two arbitrary layers, as the terms containing L_1^+ eliminate each other resulting in the following expression,

$$L_1^- = (E - R^{12}R^{10})^{-1}(R^{12}T^{01}L_0^+ + T^{21}L_2^-) \tag{3.12}$$

Similarly, an expression for the downward propagating radiance at boundary 1 can be obtained by left-multiplying R^{10} to the equation describing L_1^- (eqs. 3.10) and adding it to equation 3.8:

$$L_1^+ = (E - R^{10}R^{12})^{-1}(T^{01}L_0^+ + R^{10}T^{21}L_2^-) \tag{3.13}$$

Equation 3.13 can be substituted into the equation describing radiance through the layer with boundaries 1 and 2 (eq. 3.10) yielding the following expression for L_2^+,

$$L_2^+ = [T^{12}(E - R^{10}R^{12})^{-1}T^{01}]L_0^+ + [T^{12}(E - R^{10}R^{12})^{-1}R^{10}T^{21} + R^{21}]L_2^- \tag{3.14}$$

The above expression (eq. 3.14) is an analogous expression to the juxtaposed equation for L_2^+ (eq. 3.11). By comparing these two equations, expression describing the reflection and transmission operators for the combined layers can be obtained:

$$\begin{aligned} T^{02} &= T^{12}(E - R^{10}R^{12})^{-1}T^{01} \\ R^{20} &= T^{12}(E - R^{10}R^{12})^{-1}R^{10}T^{21} + R^{21} \end{aligned} \tag{3.15}$$

By applying a similar substitution to equation 3.9 using equation 3.12 and comparing the results to the juxtaposed equation for L_0^- (eq. 3.11), expressions for the operators T^{20} and R^{02} can be

obtained. These equations can be used repeatedly to find the reflection and transmission of an arbitrarily layered sample.

3.2.4 Layer Initialization

As described in section 3.2, the reflection and transmission functions of a sufficiently thin slab can be estimated using the single scattering equations represented by *van de Hulst* for isotropic scattering [14]. For azimuthally independent anisotropic scattering the redistribution function must be included. The following expressions represent the single scattering reflection and transmission functions for a thin layer,

$$\begin{aligned} R(a,b,v,v') &= \frac{a\pi h(v'-v)}{v'+v}\Big[1-\exp\Big(-\frac{b}{v'}-\frac{b}{v}\Big)\Big] \\ T(a,b,v,v') &= \frac{a\pi h(v'-v)}{v-v'}\Big[\exp\Big(-\frac{b}{v}\Big)-\exp\Big(-\frac{b}{v'}\Big)\Big] \end{aligned} \tag{3.16}$$

Here, the single scattering reflection and transmission are functions of sample albedo, optical thickness and incident and scattered directions of radiance (represented as a, b, v and v' respectively).

3.2.5 Boundary Conditions and Internal Reflection

At the boundaries of the sample, radiance can either by internally reflected or transmitted across the boundary, depending on its angle of incidence. This is implemented in the adding-doubling method by creating a layer which mimics the reflection and transmission at a boundary. The created layer is added to the modelled sample (slab) to find the reflection and transmission under boundary conditions. If $r(v)$ is the Fresnel reflection for light incident from a medium with index of refraction n_0 on another medium with index n_1, the reflection and transmission matrices can be written as,

$$\begin{aligned} R^{01}(v_i,v_j) &= \frac{r(v_i)}{2v_i}\delta_{ij} \\ T^{01}(v_i,v_j) &= \frac{1-r(v_i)}{2v_i}\Big(\frac{n_1}{n_0}\Big)^2\delta_{ij} \end{aligned} \tag{3.17}$$

The reflection function $r(v_i)$ is the unpolarized Fresnel reflection function. The Kronecker delta function makes both reflection and transmission matrices diagonal, ensuring that light is specularly

reflected at angles equal to incident angles. Similarly, the reflection and transmission operators for randiance moving from medium 1 into medium 0 can be given as,

$$\begin{aligned} R^{10}(v_i, v_j) &= R^{01}(v_j, v_i) \\ T^{10}(v_i, v_j) &= T^{01}(v_i, v_j)\left(\frac{n_0}{n_1}\right)^2 \delta_{ij} \end{aligned} \tag{3.18}$$

3.2.6 Implementation

The general steps in the implementation of the adding-doubling method for calculating the reflection and transmission through a turbid slab with the medium having a index of refraction, consists of the following steps:

- Choosing quadrature scheme.
- Initializing starting layer.
- Generating boundary layers.
- Doubling starting layer until desired thickness is researched.
- Incorporating boundary layers.
- Calculating overall reflection and transmission of the modelled sample.

A user-friendly verison of the adding-doubling algorithm has been developed by *Prahl*, and has been used by the inverse adding-doubling algorithm to accomplish inverse calculations of optical properties from measurements of reflection and transmission from samples [13, 26]. Furthermore, this program has optimized to run under MATLAB's environment (see appendix B).

3.3 Error Metric for Inverse Calculations

With the reflection and transmission values calculated by the adding-doubling, a metric to understand how far these values are to experimentally measured values, is required. According to *Prahl et. al*, the best metric is a sum of relative errors of both reflectance and transmittance values, as described below,

$$M(a,b,g) = \frac{|R_{AD} - R_{IS}|}{R_{IS} + 10^{-6}} + \frac{|T_{AD} - T_{IS}|}{T_{IS} + 10^{-6}} \tag{3.19}$$

here R_{IS} and T_{IS} are the reflectance and transmittance measured using an integrating sphere, while R_{AD} and T_{AD} are the AD calculated reflectance and transmittance values, respectively. The factor of 10^{-6} is introduced to prevent a division by zero in cases where measured values may be zero.

3.4 Iteration Mechanism for Inverse Calculations

The iteration mechanism incorporated in the IAD is an N-dimensional minimization algorithm based on the downhill simplex method proposed by *Nelder and Mead* [27]. The AMOEBA implementation of this scheme, varied the parameters from $-\infty$ to ∞. Since the input optical parameters (a, b, g) all have fixed ranges, the will be transformed into this computation space. For example, the sample albedo can be transformed as follows,

$$a_{comp} = \frac{2a-1}{a(1-a)} \tag{3.20}$$

Through this transformation, the a_{comp} varies within the limits of $-\infty$ to ∞. A similar transformation can be applied to the other two optical parameters as follows.

$$b_{comp} = \ln(b) \qquad g_{comp} = \frac{g}{1+|g|} \tag{3.21}$$

These values can be inverted to obtain the real optical parameters easily. These transformations were only used by the simplex method, for choosing the next iteration point. With these implementations, the IAD typically takes within 20-30 iterations to converge to a solution, for a set of R_t and T_t measurments.

3.5 IAD error analysis - Accuracy

Before incorporating the IAD method to estimate optical properties of any unknown media, one fundamental question must be answered - How precise and accurate is the IAD in the derivation of optical properties if the total reflectance and transmittance of a sample are exactly known? Due to the unavailability of analytical expressions that describe light propagation in media with mismatched boundaries, the error analyses must be done numerically.

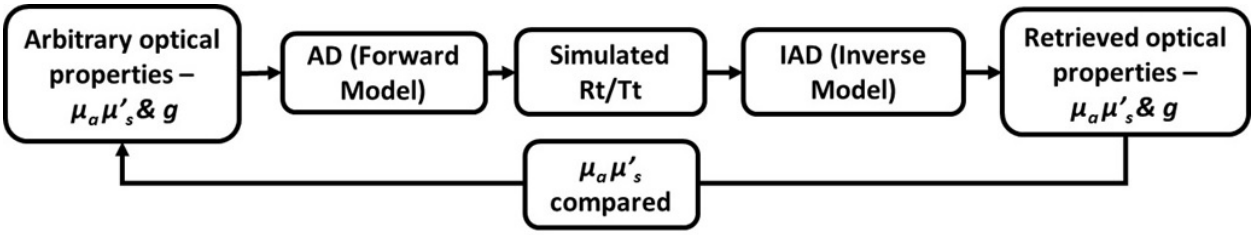

Figure 3.3: Schematic representation of the protocol for error analysis

The accuracy of the IAD can be probed numerically using a set of arbitrary optical properties that emulate tissues ($0.1cm^{-1} < \mu_a < 4cm^{-1}$ and $1cm^{-1} < \mu'_s < 45cm^{-1}$). The total reflectance and transmittance for these optical properties can be estimated using the AD (forward model). These estimated values can then be given to the IAD (inverse model) as inputs to retrieve the original optical properties, allowing one to quantify the performance of the inverse model. Figure 3.3 is a schematic describing this process.

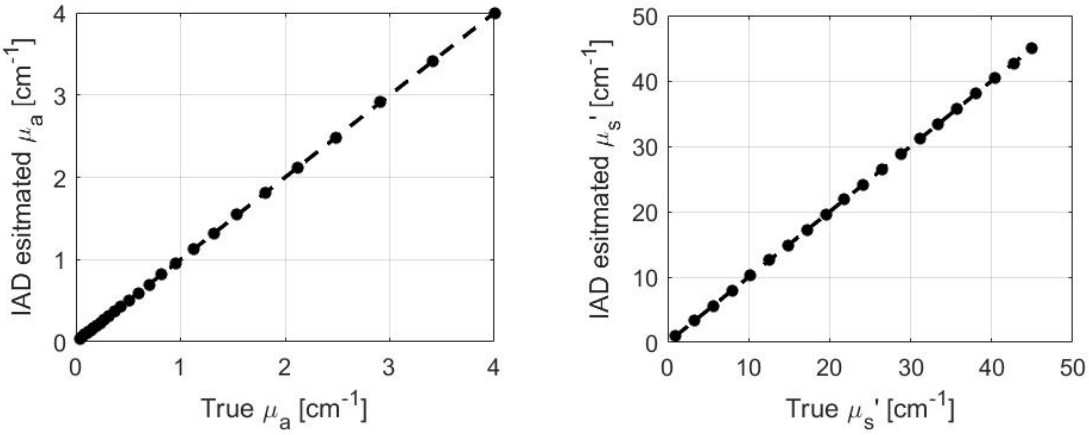

Figure 3.4: Validation of the IAD method in estimation of optical properties for a set of arbitrary optical properties. The mean relative errors in estimated absorption (left) and scattering (right) are within 0.05%.

For the range of optical properties used in these simulations (i.e. ranges analogous to tissue optical properties specified above), it can be observed that the retrieved absorption and scattering values have a maximum relative errors of up to 0.175% and 0.036%, respectively. It must be noted that absorption values are slightly more that the scattering estimates.

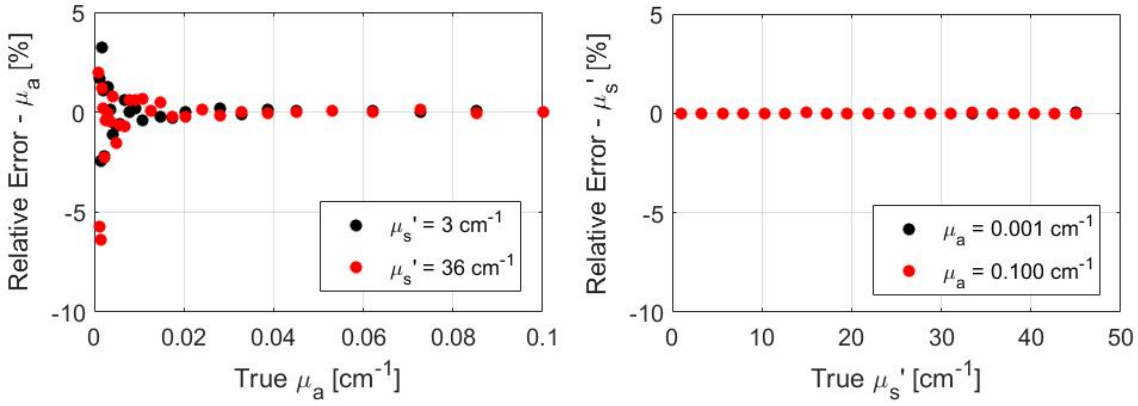

Figure 3.5: Relative errors in IAD estimated optical properties from true optical properties. Describes the ranges of optical properties where the IAD fails to predicted the true optical properties. On the left figure, the black and red dots represent two levels of scattering for all absorption data points. On the right figure, the black and red dots represent two levels of absorption for all scattering data points (This labelling scheme is followed for following plots in this chapter).

Figures 3.5 are plots of relative errors of IAD retrieved optical properties compared to the ”true” optical properties used as inputs to the analysis protocol described in figure 3.3. It can be observed that the errors in the IAD estimated scattering remain negligible though absorption levels for these data points have changed. On the other hand, the IAD estimated absorption breaks down for absorption values below $0.02\,cm^{-1}$, with relative errors up to $8\,\%$. Hence, one must ensure that absorption coefficients of the samples measured using the IS/IAD technique have absorption values over this threshold.

3.6 IAD error analysis - Sensitivity

To run an inverse calculation using the IAD, some important sample and system parameters are required (see appendix A.1). By perturbing these parameters, their effects on the inverse calculations can be quantified. In the following sections, the sensitivity of the IAD to perturbing parameters such as, the total reflectance and transmittance, anisotropy, sample index, sphere wall reflectivity, and glass index, and their effects on the inverse calculated optical properties are presented.

3.6.1 Total Reflectance and Transmittance

The total reflectance and transmittance are the two fundamental measurements made on any sample (as mentioned in section 2.1). However, perturbations to these values can occur due to detector

capabilities or fluctuations in the source. This can be modelled by perturbing the values to total reflectance and transmittance given to the IAD in the workflow described in figure 3.3, allowing one to quantify the errors in the inverse calculations. For the detector used for measuring phantoms in this thesis (see chapter 2 and 4), the variance in measurements are within or below the third decimal place (± 0.001). Hence, by perturbing the input reflectance and transmittance by $+0.001$, the sensitivity of the IAD to these inputs will be explored.

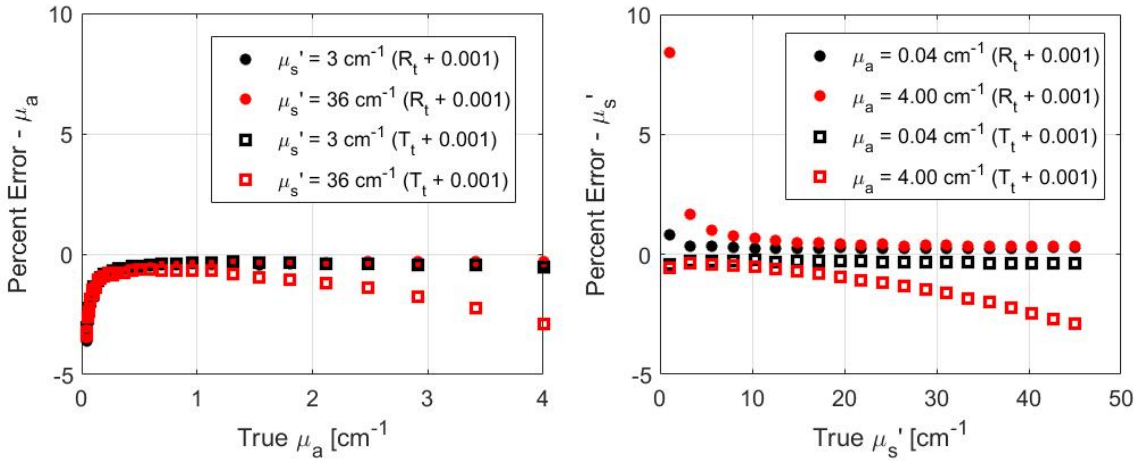

Figure 3.6: The effects of perturbing the input reflectance and transmittance by $+0.001$, on estimated optical properties. The solid spheres and hollow squares represent perturbations to input reflectance and transmittance, respectively.

Figure 3.6-left describes the relative errors in IAD estimated absorption coefficients and it can be observed, the perturbation to the measurements (reflectance or transmittance) significantly affects the estimation of lower absorption coefficient ($\approx < 0.5\,cm^{-1}$) irrespective of the scattering of the sample. For a highly scattering sample, the perturbations to the total transmission seems to have a significant affect to the overall estimation of absorption values as well. Figure 3.6-right describes the relative errors in IAD estimated reduced scattering coefficients. In contrast to the observations of the absorption errors for perturbed transmission values, the overall estimation of scattering is affected for a sample with high absorption. These observations can be a result a 0.001 perturbation being a significant percent of the measured transmittance at the higher absorption and scattering limit. Furthermore, we observe the highest relative errors for lower scattering samples ($< 0.5\,cm^{-1}$).

3.6.2 Anisotropy

The inverse calculations assumes, implicitly, that a unique combination of absorption, scattering and anisotropy determine any given reflectance and transmittance measurements. As described in section 3, the IAD requires an initial guess of optical properties of the sample to run further inverse iterations. If an accurate unscattered transmittance measurement can be made, the anisotropy can be estimated using the Henyey-Greenstein function (section 1.3.1). Alternatively, an initial guess of the sample anisotropy can be provided to initiate inverse calculations by the model. By slightly perturbing the initial guess of g, its significance in the inverse calculations can be quantified.

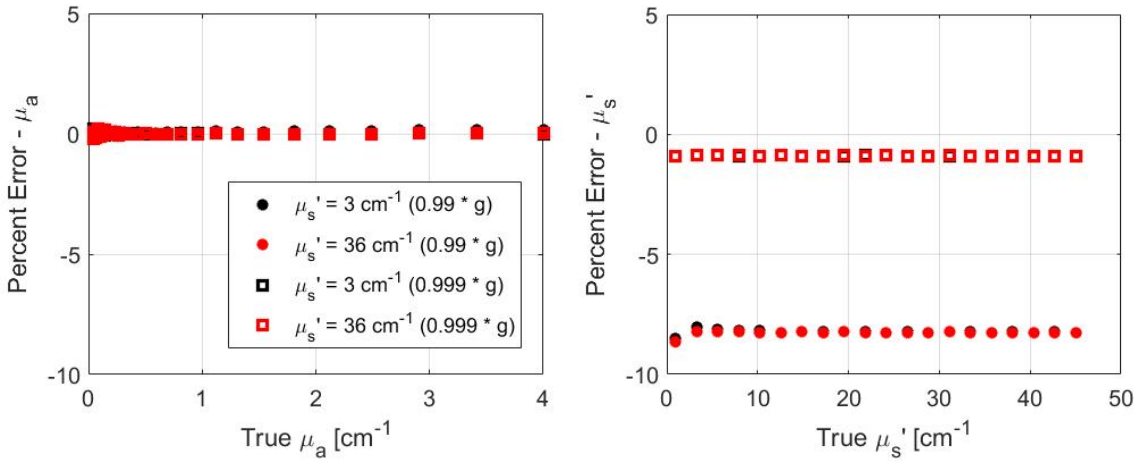

Figure 3.7: The effects of perturbing the initial guessed anisotropy by 0.1% (hollow squares) and 1% (solid spheres) on estimated optical properties.

Perturbation of the initial guess of anisotropy seems to have little to negligible effect on the inverse calculated absorption values, with maximum relative errors limited to 1 % (Fig. 3.7-left). On the other hand, the effect on calculated reduced scattering values are more significant with errors up to 10 % when initial guess for anisotropy is perturbed by 1 % (Fig. 3.7-right). Hence, one must ensure that the initial guess for absorption values are accurate to within 1 %.

3.6.3 Sample Index

The next important parameter required by the IAD, is the optical refractive index of the sample. The refractive index is a wavelength depending parameter that is generally averaged to a single value. This is due to the wavelength dependent variations typically being limited to the third decimal place. However, for the purposes of the IAD calculations, the sample index is still treated as a single value. Here, by perturbing the sample index in the third decimal place ($\pm$0.001), the

sensitivity of the IAD to the sample index and the need the need to vary the index as a function of wavelength can be determined.

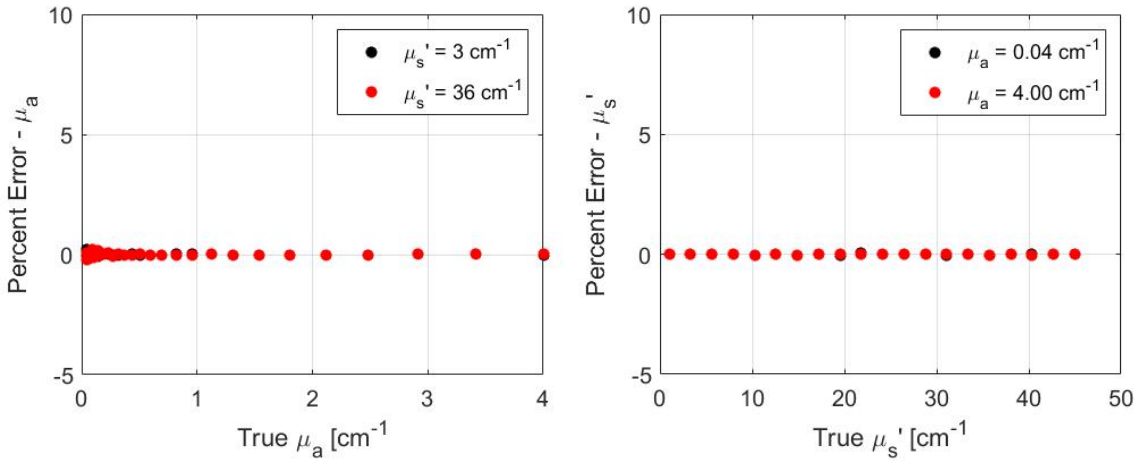

Figure 3.8: The effects of varying input sample index by 0.1 %, on estimated optical properties. The highest mean relative errors in estimated absorption (left) and reduced scattering (right) across the range of simulated optical properties are limited to within 1%.

As observed in figure 3.8, the maximum relative errors on the inverse calculated optical properties are limited to within 1 % for both absorption and reduced scattering for the range of optical properties simulated here. From these observations, it can be concluded that using an average value of the wavelength depended sample index is appropriate as the IAD is agnostic to variations in the third decimal of the sample refractive index.

3.6.4 Sample thickness

Accurate measurements of the sample thickness is vital to estimating optical properties. In applications of Beer-Lambert's law, the intensity of a sample falls exponentially with the sample thickness. A crude 1 % perturbation of the sample thickness to Beer-Lambert's law (eq. 4.1), results in a 1 % relative error overall. In this subsection, the sensitivity of the IAD to the input sample thickness will be explored by performing a similar perturbing to the input sample thickness (by 1 %). The IAD estimated optical properties will then be compared to true values.

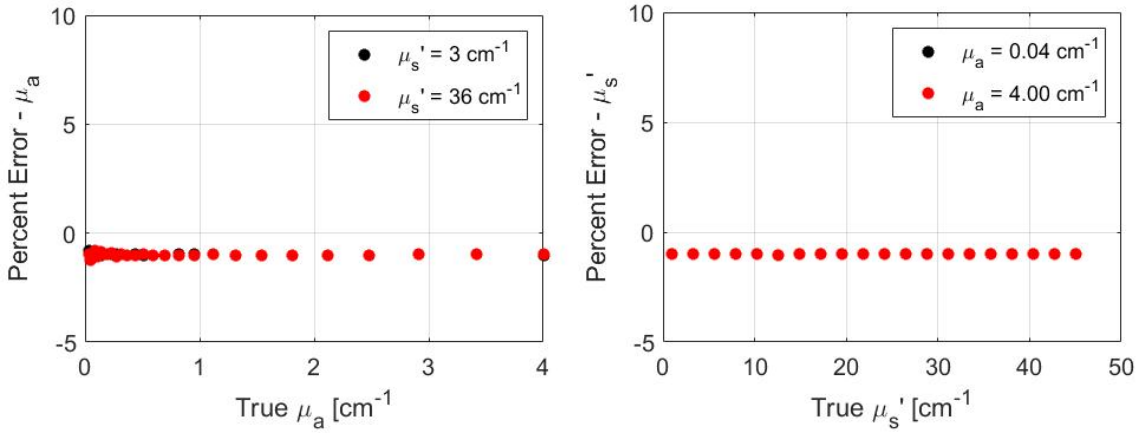

Figure 3.9: The effects of varying input sample thickness by 1 %, on estimated optical properties. This perturbation corresponds to a change of 0.001 *cm* to the sample thickness. A uniform relative error of 1 % can be observed over all calculated optical properties.

Figure 3.9 describes the relative errors in the IAD calculated optical properties compared to the true optical properties provided as inputs to the error analysis (described in fig. 3.3). As observed, irrespective of the optical properties used for these error analyses, there remains an overall 1 % error in the calculated optical properties. Hence, if an accuracy, within this threshold is desired, an accurate measurement of the sample thickness must be provided to the IAD.

3.6.5 Index of Ambient Medium

The final parameter required by the IAD to run inverse calculations is the refractive index of the ambient medium surround the modelled tissue. Similar to the investigations on the sample refractive index, the index of the ambient medium will also be perturbed in the third decimal place and the calculated optical properties will be compared to the true optical properties.

As observed in figure 3.8, the maximum relative errors on the inverse calculated optical properties are limited to within 1 % for both absorption and reduced scattering for the range of optical properties simulated here. From these observations, it can be concluded that using an average value of the ambient refractive index is also appropriate as the IAD is agnostic to variations in the third decimal of the ambient index.

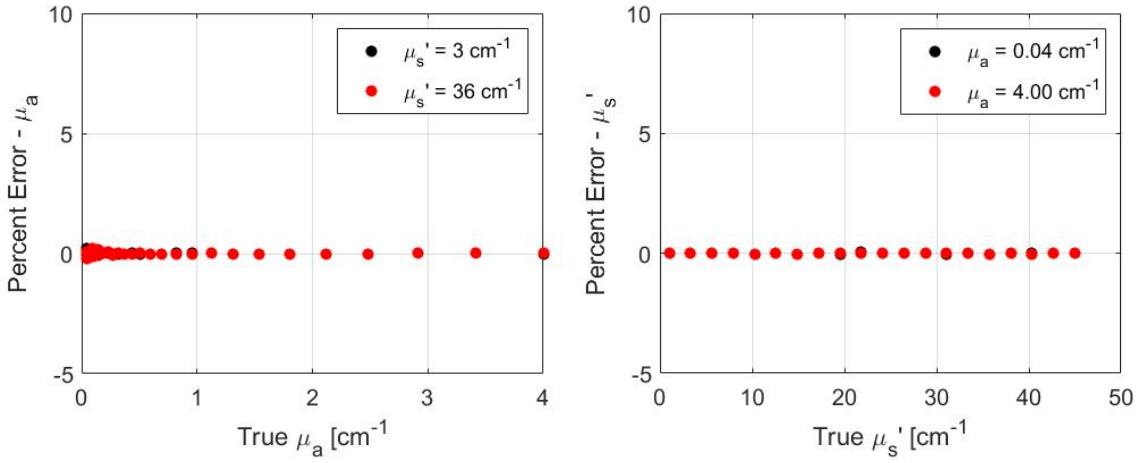

Figure 3.10: The effects of varying the index of refraction of the ambient medium by 0.1 %, on estimated optical properties. The highest mean relative errors in estimated absorption (left) and reduced scattering (right) across the range of simulated optical properties are limited to within 1%.

3.7 Summary

In this subsection, I have summarized all the results of the accuracy and sensitivity analyses performed in this chapter. Table 3.1, lists the maximum relative errors of the IAD estimated optical properties and the range of input optical properties (μ_a, μ_s') where they are observed, for the tests conducted in this chapter.

R_t	T_t	g	n_{sample}	$d(cm^{-1})$	n_{glass}	Error (μ_a)		Error (μ_p')	
						%	μ_a, μ_s'	%	μ_a, μ_s'
R_{ad}	T_{ad}	0.900	1.330	0.200	1.550	0.042	-	0.011	-
$R_{ad} + 10^{-3}$	T_{ad}	0.900	1.330	0.200	1.550	5.900	0.04, 1	8.400	4, 1
R_{ad}	$T_{ad} + 10^{-3}$	0.900	1.330	0.200	1.550	5.550	0.04, 1	2.910	4, 45
R_{ad}	T_{ad}	0.899	1.330	0.200	1.550	0.042	-	0.011	-
R_{ad}	T_{ad}	0.891	1.330	0.200	1.550	0.042	-	8.600	4, 1
R_{ad}	T_{ad}	0.900	1.331	0.200	1.550	0.042	-	0.011	-
R_{ad}	T_{ad}	0.900	1.330	0.202	1.550	1.260	-	1.025	-
R_{ad}	T_{ad}	0.900	1.330	0.200	1.552	0.042	-	0.011	-

Table 3.1: Table summarizing the results of the IAD Error anslyses performed in sections 3.5 and 3.6.

Chapter 4

Sample Measurements using IS/IAD

Before implementing the IS/IAD method to estimate optical properties of unknown media, the accuracy of the method must be understood. This can be done using samples whose optical properties can be controlled, precisely and accurately. Optical phantoms are such samples, comprising of known concentrations of absorbers and scatterers. By varying the concentrations of absorbers and scatterers in the sample, the bulk optical properties of the sample can be precisely controlled. Validation studies on various spectroscopic methods have been conducted using optical phantoms that are both solid and liquid in nature [1, 2, 15, 28]. This is possible due the ability to theoretically evaluate the true optical properties.

Ideally, the theoretically absorption spectra can be derived from the Beer-Lambert law by making an accurate measurement of the unscattered transmittance through a non-scattering solution of absorbers. Equation 4.1, describes Beer's law in its functional form.

$$\frac{I}{I_0} = e^{-\mu_t l} \implies \mu_a = -\frac{1}{l}\ln\left(\frac{I}{I_0}\right) \tag{4.1}$$

where, $\mu_t = \mu_a$ for a purely absorbing solution of path length l with $\frac{I}{I_0}$ being the fraction of unscattered light transmitted through the sample (total unscattered transmission). Accurate measurements of unscattered transmission can be made using a UV-VIS spectrophotometer [1, 8, 15].

The scattering and anisotropy coefficients of optical phantoms can be theoretically evaluated using Mie theory. Mie theory solutions to the Maxwell's equations describes scattering of a monochromatic electromagnetic wave by a suspension of homogeneous spheres of a finite radius [11]. With knowledge of certain parameters (such as concentration and distribution of sphere) of the scattering solution, the scattering and anisotropy coefficients can be analytically computed [29].

4.1 Liquid phantoms

For the purposes of this thesis, the validation of the IS/IAD method's ability to estimate optical properties will be quantified using a robust set of liquid phantoms. The properties of these phantoms will span absorption, scattering and anisotropy coefficients typical to common biological tissues in the VIS spectral range [1]. These phantoms were prepared and measured on the same day, to ensure the integrity of the samples did not change. Furthermore, the homogeneity of the sample was reinforced by firmly mixing the solutions prior to measurements.

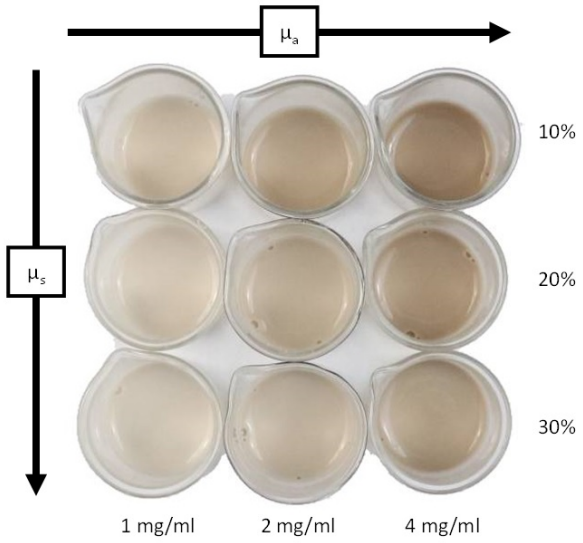

Figure 4.1: 3x3 set of phantoms used for preliminary analyses. Moving from top to bottom, the scattering of the sample is increased by 10% increments, while absorption increases moving left to right is doubled by a factor of 2.

The first set *(referred as Dataset I)* of liquid phantoms used in these studies comprise of three levels of concentrations ($1mg/ml$, $2mg/ml$ and $4mg/ml$) of Bovine hemoglobin (*Sigma-Aldrich H3760*) as aborbers. As scatterers of these phantoms, three concentrations levels (10%, 20% and 30%) of $1\mu m$-polystyrene sphere suspension in solution is used (*Polysciences Polybead® 07310*). As seen in figure 4.1, a set of 9 liquid phantoms with these three levels of absorption and scattering is developed. The "true" optical properties of these samples are calculated using the methodologies described in chapter 4.

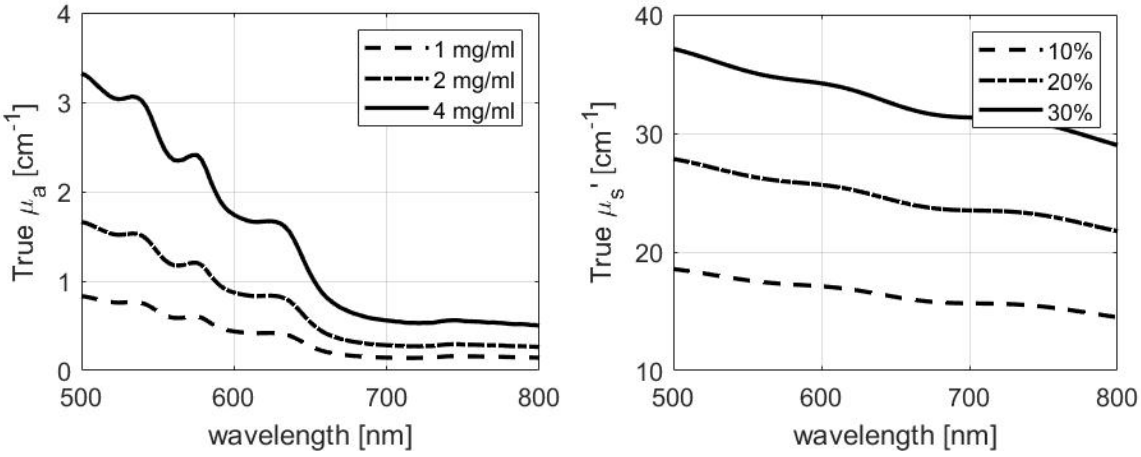

Figure 4.2: Plots of true absorption coefficient (left) and scattering coefficient (right) spectra for the 9 phantoms (described in fig. 4.1), calculated using Beer-Lambert law and Mie theory, respectively.

Figures 4.2, describes the "true" optical properties of the samples described in figure 4.1. The characteristic spectral pattern observed in the absorption spectra (fig. 4.2-left) is typical for hemoglobin and can be observed in common biological tissues. It must be noted that the lowest absorption values in this dataset are well beyond the thresholds of the IAD to estimate properties accurately ($> 0.1\,cm^{-1}$). **The second set** *(referred as Dataset II)* of phantoms comprise of varied concentrations of $1\mu m$ polystyrene spheres in water. The concentrations of these phantoms is described in table 4.1,

Sample	1	2	3	4	5	6	7	8	9	10
PS	30%	24%	19.2%	15.4%	12.3%	9.8%	7.9%	6.3%	5.0%	4.0%

Table 4.1: Second dataset of multiple concentrations polystyrene sphere solutions.

The true optical properties of these phantoms are plotted in figure 4.3. Corresponding to the volume percent of polystyrene in solution for each individual sample, the reduced scattering spectra can be described using Mie theory. However, the total absorption coefficient of these samples will be that of water as there is no other absorbers in solution. Various studies have been conducted to characterize absorption of water over the VIS spectral region and an aggregate of these values are used [30]. Since the true absorption values of water falls below the thresholds of the IAD (fig. 3.5), we will only look at IAD estimated values above 730.

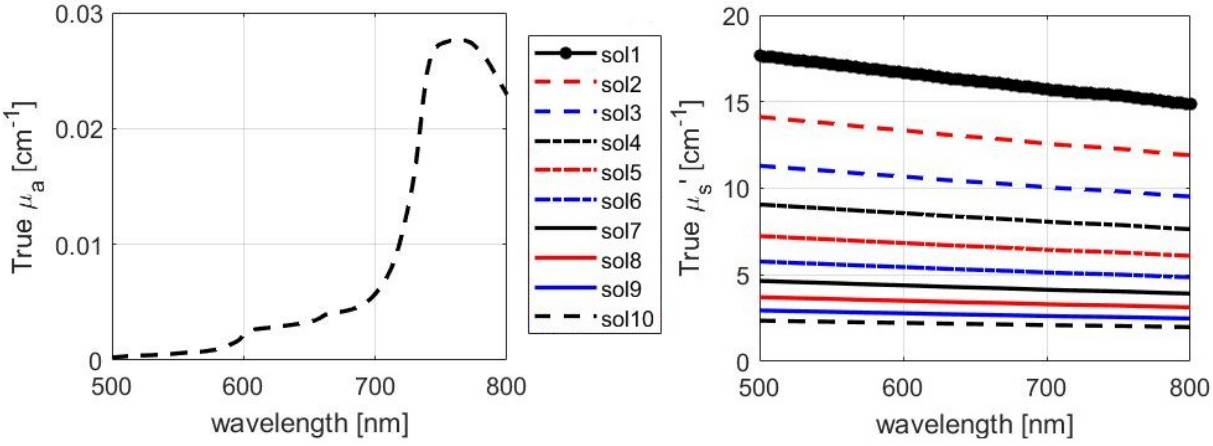

Figure 4.3: Water and PS phantoms (Dataset II) with concentrations corresponding to those represented in table 4.1.

4.2 Analysis of sample measurements

As described in chapter 2, a simple single IS setup can be built by coupling a detector to measure reflectance and transmittance intensity spectra for a given sample illuminated by a given source. This source can either be monochromatic or a broadband source. For our preliminary investigations, a broadband continuous-wave halogen source coupled with the IS will be used to make sample measurements. As described in equations 2.1, a dark and standard measurement is made with five repetitions.

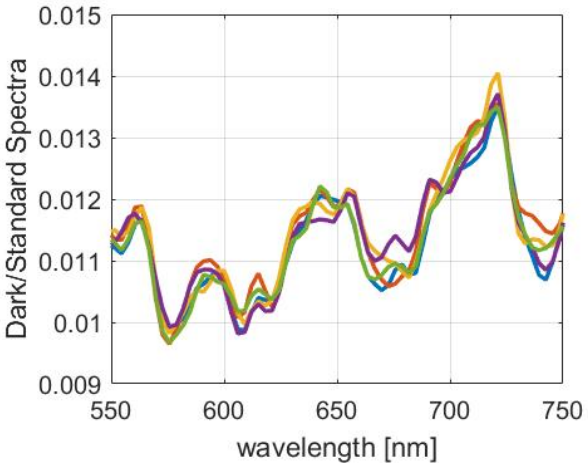

Figure 4.4: A ratio of IS measured intensity spectra with the source turned off and the intensities reflected off a reflectance standard.

Figure 4.4 is a plot of standard intensity spectra divided by the dark intensity spectra. From these plots, the sensitivity of the used spectrometer is observed within 0.001 values of IS measurements. Through the sensitivity analysis of the IAD to various inputs, we concluded that the algorithm is most sensitive to the input measurements of total reflectance and transmittance (Table 3.1). Hence, one must ensure that all IS measurements

are accurate to within 0.001 of the expected measurements. This can be done by providing the true sample optical properties to the forward adding-doubling algorithm and calculate the expected total reflectance and transmittance of all the samples analyzed. The calculated values can then be compared to the IS measurements.

4.2.1 Analysis of dataset I

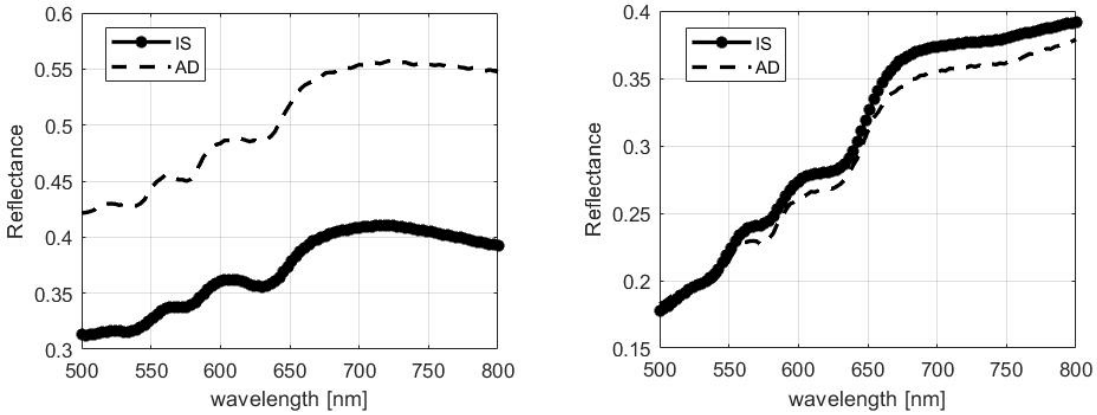

Figure 4.5: Comparison of the AD predicted total reflectance (left) and transmittance (right) with IS measured values of sample 1 - Dataset 1 (10% PS and $1 mg/ml$ Hb solution).

Figure 4.5 are plots of IS measurements against values estimated using the forward model (AD). A preliminary observation indicates that the total reflectance measurements experience a significant loss compared to the AD estimated values. Conversely, at certain wavelengths, the total transmittance values are higher than the AD simulated values, with overall differences significantly lower that those experienced by reflectance measurements. The data visualization scheme applied in the previous section, can be incorporated here to understand the performance of the IS measurements. By sampling the AD calculated measurements at every $2 nm$ intervals, a distribution of varying reflectance and transmittance can be obtained. Figure 4.6 describes the distribution of these data points across the corresponding AD calculated values and are grouped across each 0.5 intervals.

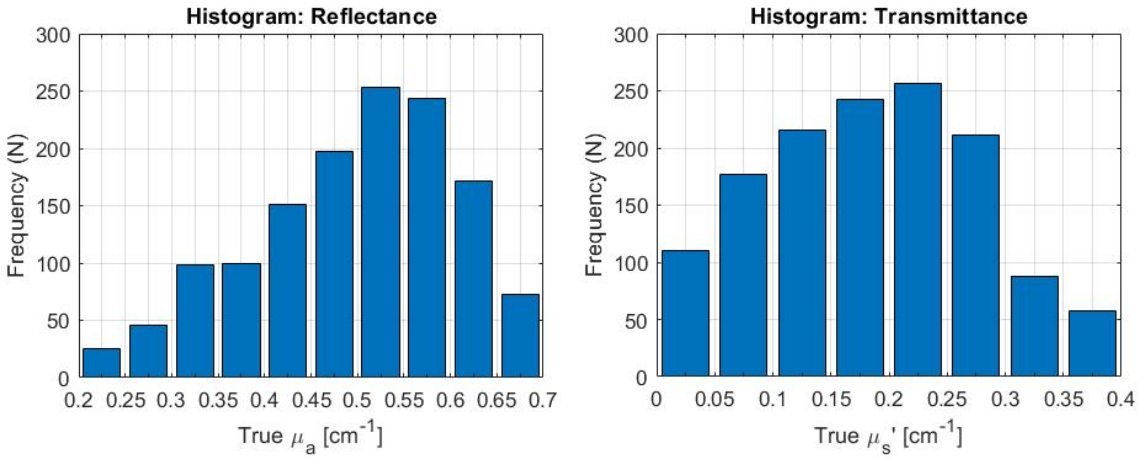

Figure 4.6: The number of data points sampled between each 0.05 reflectance (left) and and transmittance (right) ranges of all phantoms in dataset I.

Figure 4.7 describes the relative errors between IS measurements against AD predicted measurements. The highest relative errors (22%) in the IS measured reflectance values can be seen at the lower reflectance measurements ($\approx$ 0.2) (Fig. 4.7-left). These reflectance values typically correspond to samples with low reduced scattering and high absorbing coefficients.

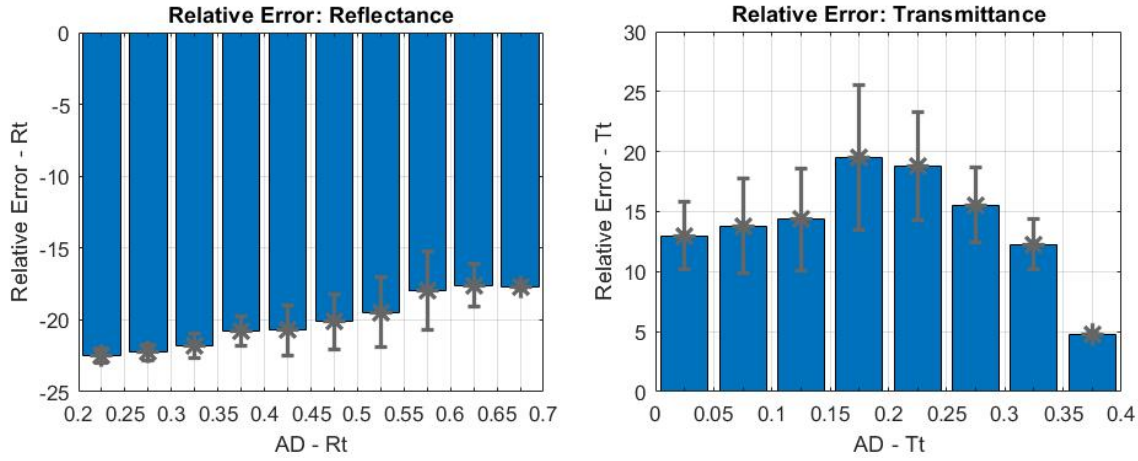

Figure 4.7: Relative errors between IS measured reflectance (left) and transmittance (right) of samples in dataset I against AD calculated values grouped in each 0.05 measurement intervals.

The highest relative errors ($\approx$ 20%) in the IS measured transmittance values can be seen at reflectance measurements within the ranges of $0.15 - 0.25$ (Fig. 4.7-right). It must be noted that the these ranges are similar to that of highest errors in reflectance measurements.

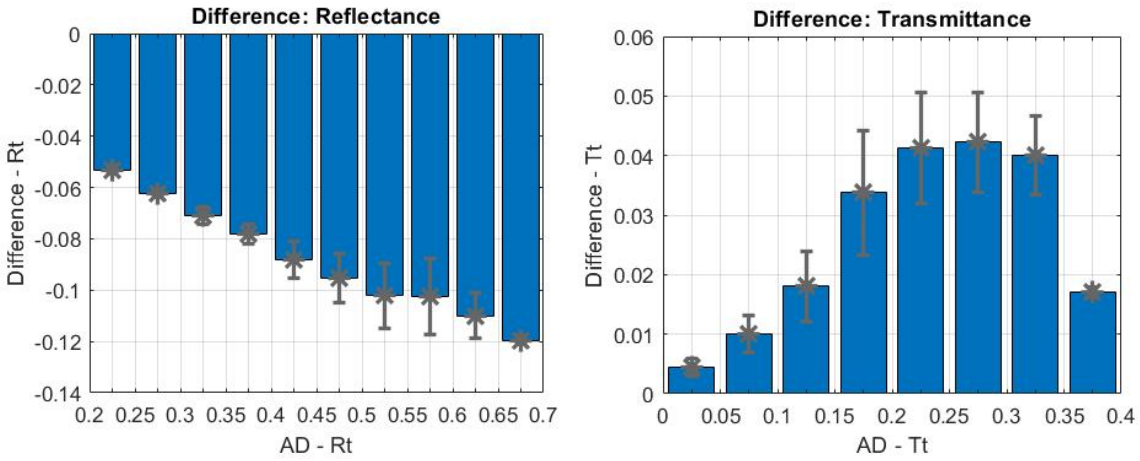

Figure 4.8: Difference between IS measured reflectance (left) and transmittance (right) of samples in dataset I against AD calculated values grouped in each 0.05 measurement intervals.

The differences the IS measurements against AD calculations are plotted in figure 4.11. As more light is collected by the sphere for reflectance measurements, a greater magnitude of light is lost in these measurements (Fig. 4.11-left). Conversely, the greatest light losses are observed for measurements within intervals $0.2-0.3$ total transmittance. It must be noted that light losses in total reflectance measurements are $\approx 10\times$ that of losses observed in total transmittance values. The resolution of the IS to make measurements of total reflectance and transmittance can be estimated by averaging the differences described above. Here, the resolution of the IS to make measurements of total reflectance and transmittance for dataset I are 0.078 and 0.018, respectively.

4.2.2 Analysis of dataset II

Dataset II covers a wider range of absolute values of reflectance and transmittance measurements. Hence, this data will be grouped into each 0.1 intervals of measurements and the trends across these ranges will be observed. Figure 4.9 plots the distribution of these sampled data points across all measurements made on samples in dataset II. It must be noted that this distribution spans the lower refleactance $(0-0.1)$ and higher transmission $(0.9-1)$ values.

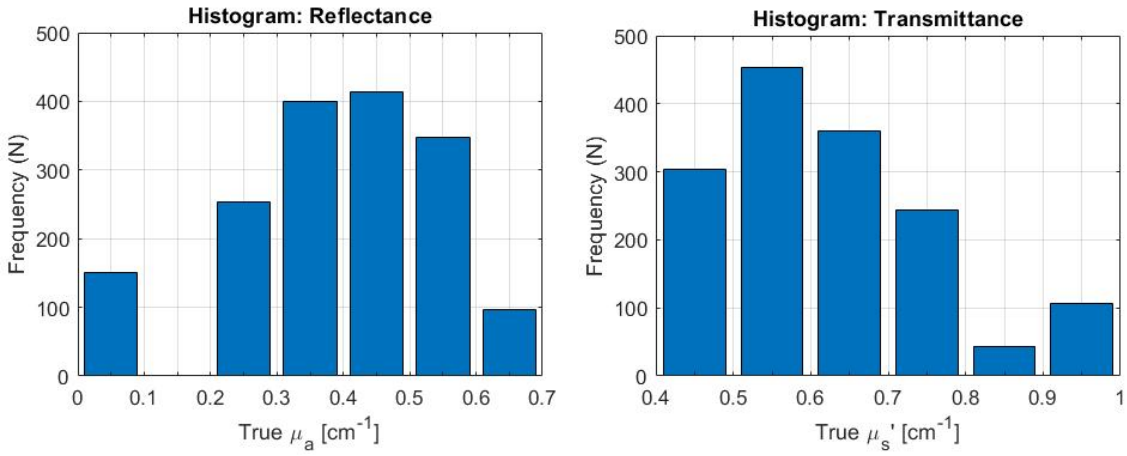

Figure 4.9: The number of data points sampled between each 0.1 reflectance (left) and and transmittance (right) ranges of all phantoms in dataset II.

Figure 4.10 describes the relative errors in IS measurements against AD calculated values. As observed, the highest errors in reflectance measurements can be observed in the ranges of $0.2-0.3$, similar to the observations in dataset I (Fig. 4.10-left). On the other hand, the highest relative errors for transmittance measurements can be observed for the ranges $0.6-0.7$, which is different from the observations seen above. It must be noted that at higher transmission values $(0.8-1)$ positive relative errors can be observed.

When observing the differences between IS measurements against AD calculations, it can be observed that, consistent with the observations for dataset I, the IS measured reflectance values experiences losses throughout all measured values. However, the difference remains to be significant in the $0.5-0.7$ region. Conversely, the magnitude of the transmittance measurements is lower overall with the highest difference of ≈ 0.08 within the $0.7-0.8$ interval. However, within the intervals of $0.9-1$, the IS measured transmittance values are greater than those calculated through the AD. Here, the resolution of the IS to make measurements of total reflectance and transmittance for dataset II are 0.139 and 0.044, respectively.

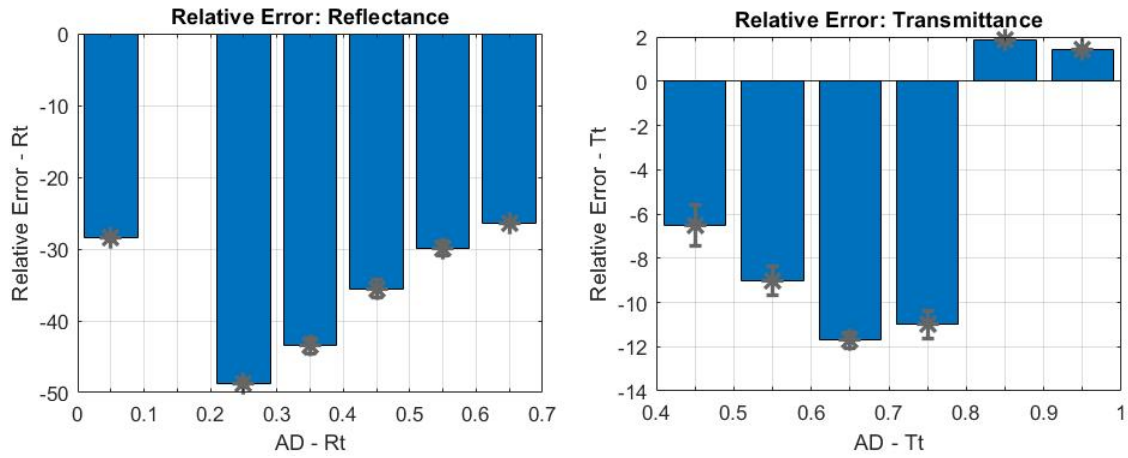

Figure 4.10: Relative errors between IS measured reflectance (left) and transmittance (right) of samples in dataset II against AD calculated values grouped in each 0.1 measurement intervals.

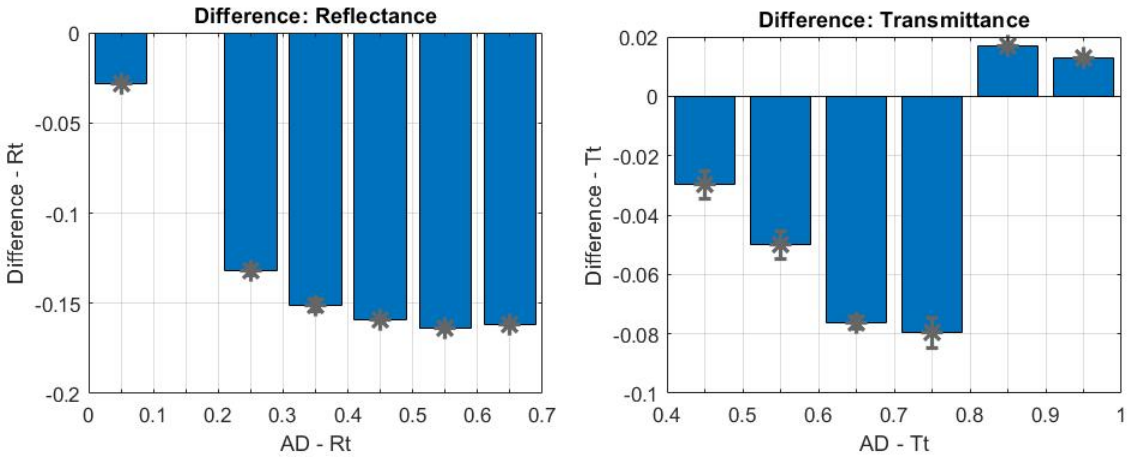

Figure 4.11: Difference between IS measured reflectance (left) and transmittance (right) of samples in dataset II against AD calculated values grouped in each 0.1 measurement intervals.

4.3 Calculation of optical properties

The IS measurements obtained above can be used to inverse calculate optical properties. Here, all other inputs to the IAD are accurate within the sensitivity thresholds listed in chapter 3. This ensures that all errors observed in inverse calculations are attributed to the IS measurements.

4.3.1 Analysis of dataset I

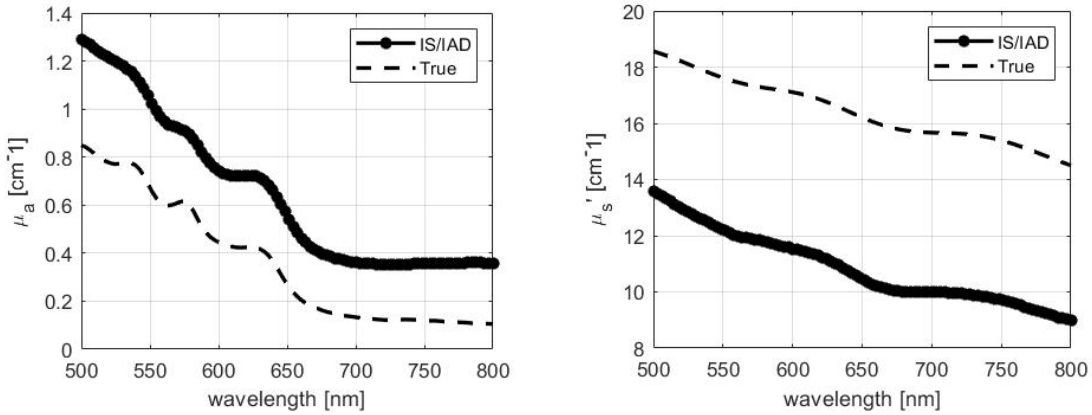

Figure 4.12: IAD estimated absorption (left) and scattering (right) coefficients of sample 1 - Dataset I (10% PS and $1 mg/ml$ Hb solution) from measurements made using an IS illuminated with a Halogen source.

Following the protocol mentioned in chapter 2, the total absorption and scattering can be calculated from IS measurement made on our optical phantoms. Figure 4.12 compares the inverse estimated absorption and scattering of sample 1 (from dataset 1) with its true optical properties. As observed, the inverse model estimates higher absorption and lower scattering values. From the conclusions summarized in table 3.1, accurate inverse estimations of optical properties is highly dependent on the ability of the IS to precisely measure the total reflectance and transmittance of any given sample. From the observations in figure 4.12, one can conclude that there is a mismatch of IS measurements with expected measurements, i.e. the true reflectance and transmittance of the sample.

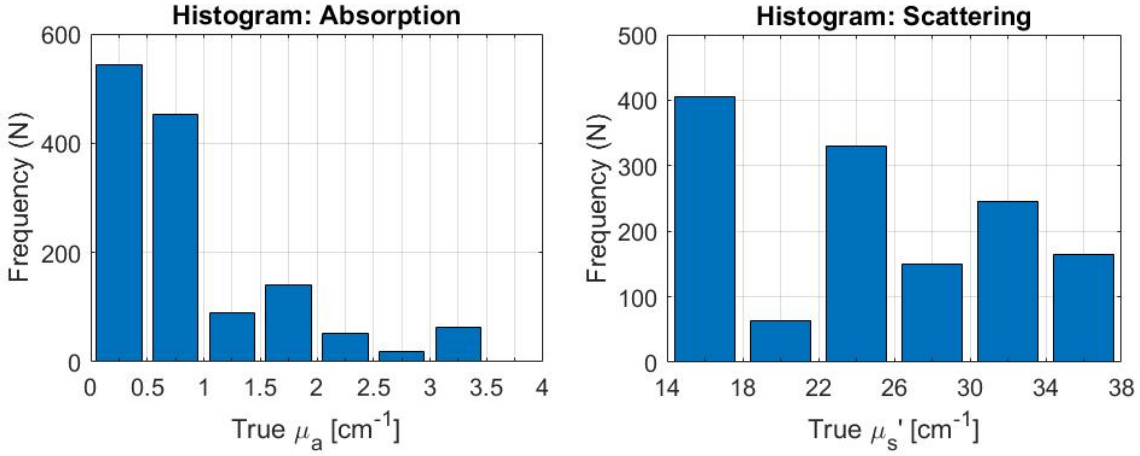

Figure 4.13: The number of data points sampled between each $0.5\,cm^{-1}$ absorption (left) and each $4\,cm^{-1}$ reduced scattering (right) ranges of all phantoms in dataset I, for error calculations.

To better visualized the performance of the IS/IAD system to estimate optical properties from phantoms illuminated by a Halogen source, all samples from the sample set are sampled at wavelength intervals of $2\,nm$. This provides a distribution of data points across intervals of absorption and scattering coefficient values. Figure 4.13, describes this distribution of all sampled data points across each $0.5\,cm^{-1}$ absorption and each $4\,cm^{-1}$ reduced scattering intervals. As observed 4.13 - left, due to the spectra features of hemoglobin over the wavelength ranges of $500\,nm$ - $800\,nm$ (Fig. 4.2-left), we observe most of the sampled absorption data points to be within the ranges of $0-1\,cm^{-1}$. Similar distributions in the sampled reduced scattering data points can also be observed (4.13-right).

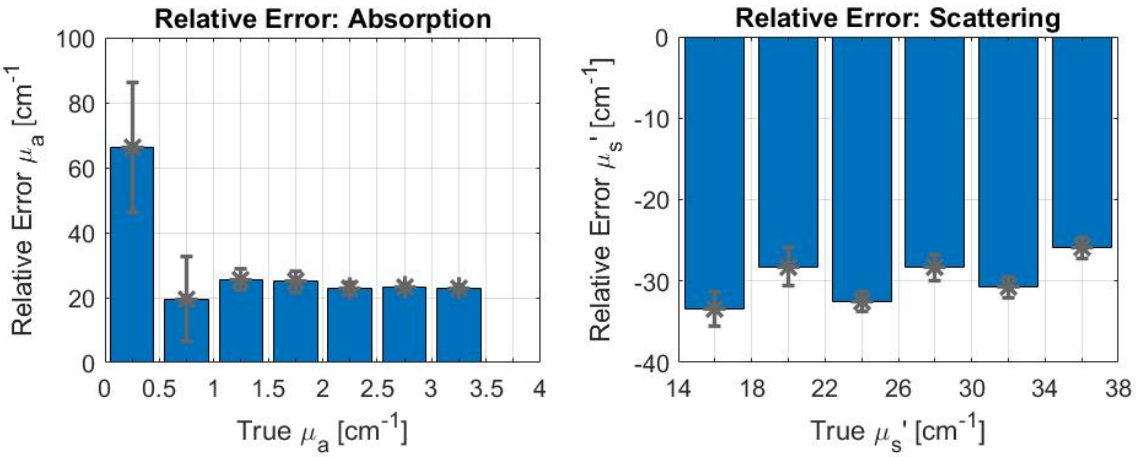

Figure 4.14: The relative errors in the IAD calculated absorption and scattering coefficients for each $0.5\,cm^{-1}$ absorption (left) and each $4\,cm^{-1}$ reduced scattering (right) ranges.

The relative errors (calculated as $E_{relative} = \frac{\mu_a(IAD)-\mu_a(True)}{\mu_a(True)} * 100$) in IAD calculated absorption and reduced scattering coefficients against true values are described in figure 4.14. As observed, over the range of optical properties measured, an overall overestimation in the absorption coefficient and underestimation in the reduced scattering coefficient can be observed. Though, an average of 25 % relative errors is observed over all ranges of reduced scattering values, there are higher variance in errors at lower values of absorption coefficients. Relative errors up to 70 % can be observed for absorption coefficient values within the range of $0-0.5\,cm^{-1}$.

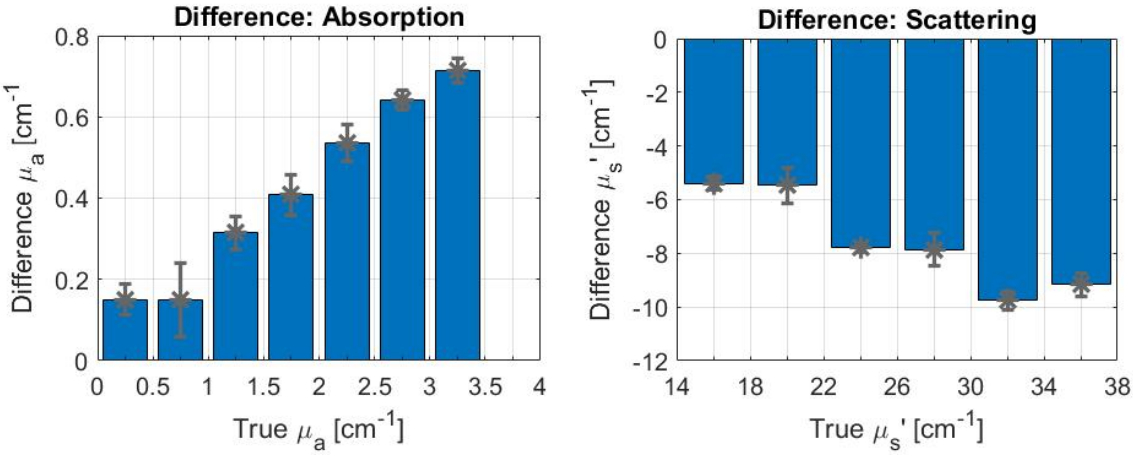

Figure 4.15: The difference between IAD calculated absorption and scattering coefficients with that of true coefficients for each $0.5\,cm^{-1}$ absorption (left) and each $4\,cm^{-1}$ reduced scattering (right) ranges.

Figure 4.15, describes the difference between IAD estimated optical properties with the "true" optical properties of the phantoms in dataset 1 (absolute errors calculated as $E_{diff} = \mu_a(IAD) - \mu_a(True)$). It is interesting to note that these differences increases with increasing absorption coefficients. A similar trend can be seen across difference in reduced scattering estimates. We can observe this minimum difference in absorption estimates to be $\approx 0.2\,cm^{-1}$, for optical properties lower than $1\,cm^{-1}$. These differences can be described as the mean resolution that the system performance over the measured range of optical properties. Here, the mean resolution of current IS/IAD configuration to estimate absorption and reduced scattering values are $0.416\,cm^{-1}$ and $7.57\,cm^{-1}$, respectively.

4.3.2 Analysis of dataset II

A similar analysis protocol will be applied to the second dataset (Dataset II). It must be noted that the true absorption and scattering values extend to lower than those explored in dataset I and has mentioned above, only values above IAD's threshold to estimate absorption values will be analyzed.

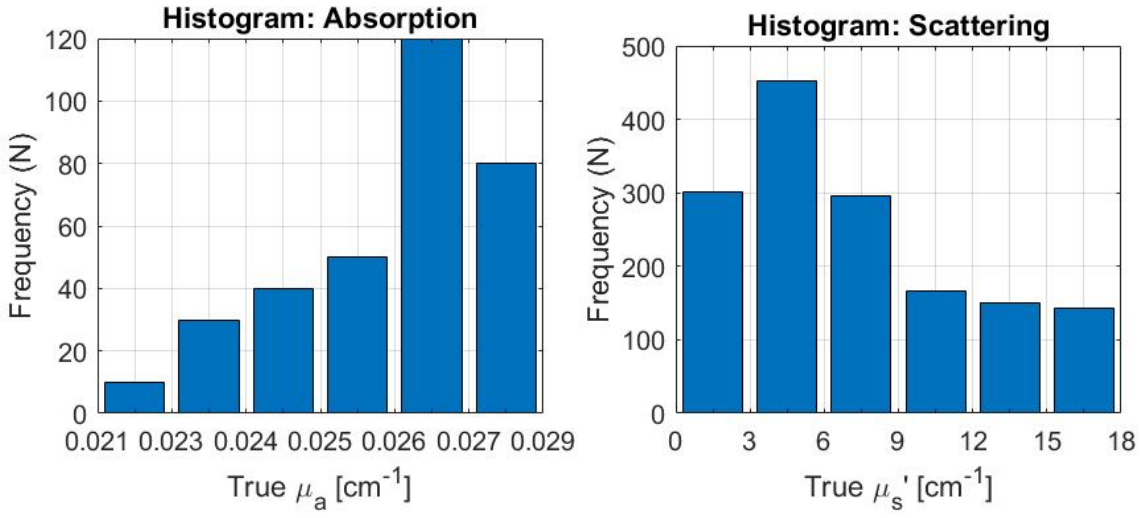

Figure 4.16: The number of data points sampled between each $0.001\,cm^{-1}$ absorption (left) and each $3\,cm^{-1}$ reduced scattering (right) ranges of all phantoms in dataset II, for error calculations.

Figure 4.16 plots the distribution of data points sampled across the absorption and reduced scattering values of the phantoms comprising dataset II. As observed, the absorption values observed will be for values greater than $0.02\,cm^{-1}$. It must be noted that the highest distribution of sampled points for absorption values are within the interval $0.026-0.027\,cm^{-1}$. Conversely, the lowest scattering values in this data set is $1\,cm^{-1}$. The highest distribution is observed, within the range $3-6\,cm^{-1}$.

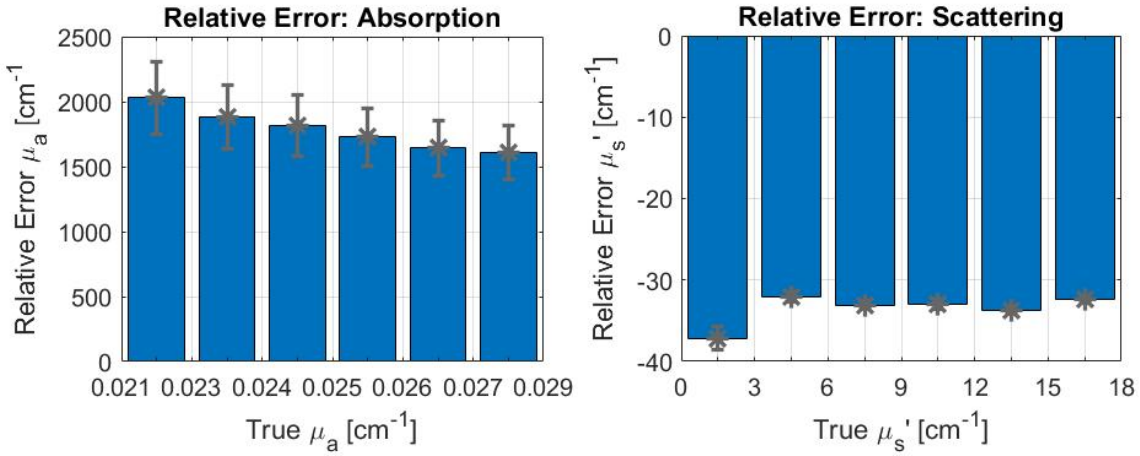

Figure 4.17: The relative errors in the IAD calculated absorption and scattering coefficients of dataset II for each $0.001\,cm^{-1}$ absorption (left) and each $3\,cm^{-1}$ reduced scattering (right) ranges.

The relative errors in the IAD estimated absorption and reduced scattering are describes in figure 4.17. As observed, the IAD estimated absorption values are meaningless as the relative errors are greater 10^4 %. The errors in the calculated reduced scattering values are similar to dataset I with an average relative errors of up to $\approx$ 35 %.

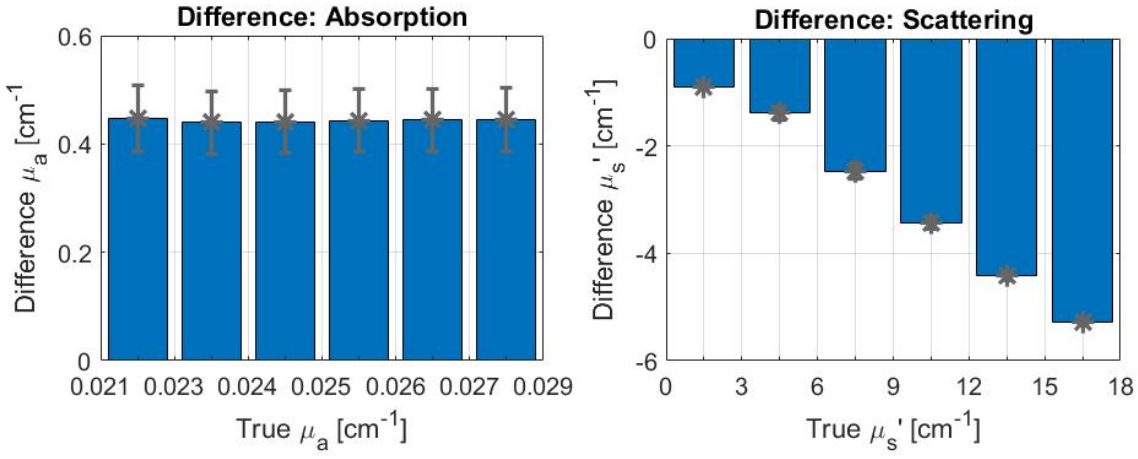

Figure 4.18: The difference between IAD calculated absorption and scattering coefficients with that of true coefficients for each 0.001 cm^{-1} absorption (left) and each 3 cm^{-1} reduced scattering (right) ranges.

Figure 4.15 describes the difference between IAD estimated optical properties against the ”true” optical properties of the sample. As observed in 4.15-left, the average difference in IAD estimated absorption is $\approx$ 0.45 cm^{-1} throughout all absorption values. These errors are greater than that observed in dataset I. On the other hand, with increasing ”true” scattering values of the sample the difference in calculated scattering is increased. Here, the mean resolution of the IS/IAD to estimate absorption and reduced scattering values in dataset II, are 0.444 cm^{-1} and 3.09 cm^{-1}, respectively.

4.4 Discussion of observations

From the preliminary experimental tests conducted on the IS/IAD technique, light losses in IS measurements of total reflectance and transmittance were observed. Here, we propose two sources of light losses to IS measurements - Lateral and hemispherical losses. As described in chapter 3, the IAD using the forward AD iteratively, to determine the optical properties of samples from IS measurements. The AD models samples to be thin infinite slabs, i.e. samples having a finite thickness across one dimension (z-direction), while extending infinitely across the other two (x & y-direction). The infinitely extending directions are those normal to the direction of photon incidence (as described in figure 4.19). However, physical tissue are not so and have finite lengths across the x & y directions. Hence, a photon incident on the surface of the sample has the probability of escaping the sample through these lateral surfaces. The AD, accounts this exiting light as absorption by the sample leading to the overestimation in optical properties by the IAD (as seen in figures 4.14 and 4.17). We name these losses as "lateral losses" and will be referred to as so for the remainder of this thesis.

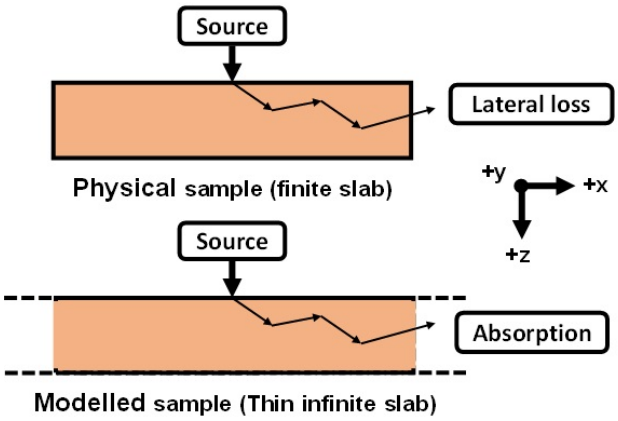

Figure 4.19: Light losses observed in IS measurements accounted as absorption by the AD method due to its thin-infinite sample model.

Integrating spheres have finite sized ports mounted through its surface. Care must be taken to ensure that the samples cover the entire surface of the sample such that all the light remitted from the sample is measured by the system. However, if the incident photon enters the sample at a position closer to the edges of the sphere port, there is a probability that the photon remitted out of the sample will not be collected within the ports of the IS (as described in figure 4.20). Theoretically, this will affect all IS measurements if the samples are il-

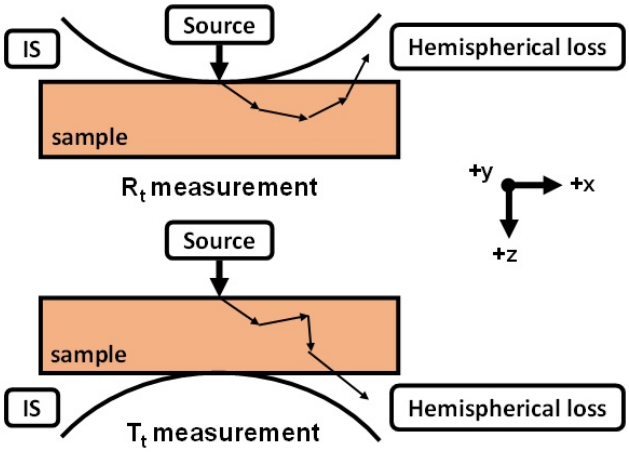

Figure 4.20: Light losses observed in IS measurements due to the finitness of IS ports

luminated by beams comparable to the size of the IS sample ports. These losses are referred to as ”Hemispherical losses”.

Integrating sphere are known to have losses in the total power collected (as described in 2.4), that arises due to the interaction between sample and sphere making the detected signal deviate from the true reflectance or transmittance of the sample. Various studies have been done to characterize the total power collected by IS with varying system configurations [10, 16, 18]. *Prahl et. al.* implemented these correction in the newest version of the IAD to improve the accuracy of all inverse calculations. Furthermore, experimental calculations to overcome these losses have also been proposed [17, 31–34]. In the next chapter, the effects light losses on varying beam, IS port and sample configurations will be explored using a robust Monte-Carlo model. This work will be concluded with exploring the performance of the theoretical and experimental corrections to realize a ”gold-standard” method of estimating optical properties.

Chapter 5

Monte-Carlo Modelling

Monte-Carlo models are stochastic methods of simulating light transport in turbid media. These turbid media are treated as substances that either absorb or scatter photons by the model [35]. The stochastic nature of the model arises by simulating photon propagation in these turbid media as a ”random-walk”. Monte-Carlo simulations have been used in various problems with laser-tissue interactions [1, 15, 36]. As a photon approaches the boundary of a modelled sample, it can be reflected or moves across the boundary. The steps between successive photon-tissue interaction sites, the deflection angles in photon trajectories (due to scattering) and the probability of transmittance or reflectance of photons at boundaries, are governed by photon propagation rules that are expressed as probability distributions. Typical photon paths observed in turbid media such as tissues are shown in figure 5.2.

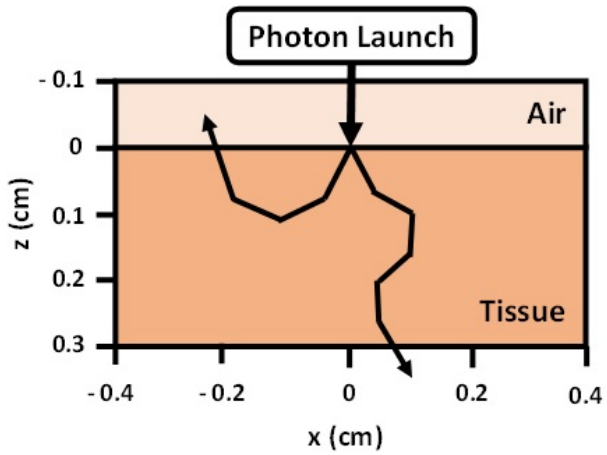

Figure 5.1: A schematic illustration of typical photon trajectories simulated by the MC model. The coordinate system displayed is typical for Monte-Carlo models, with photons launched at $z = 0$, propagating in the $+z$ direction.

The accuracy and precision to describe the desired spatial and temporal resolution is contingent on the total number of photons simulated and the specifics of the problem being addressed. For example, an accurate simulation of total reflectance for specific optical properties, would require

simulations of 3000 photons. To simulate the spatial distribution of photons in radially symmetrical problems, at least $10,000$ photons need to be simulated. Mapping photon propagation in complex three-dimensional geometries with finite beam illuminations, an average of $100,000$ photons are required. Hence, as the problems being modelled become more complex, more number of photons are required to map accurate photon propagation which significantly increases the total computational time.

5.1 General Methods

For the purposes of this thesis, the types of Monte-Carlo problems of interest are infinitely extending homogeneous tissue structures with finite thickness that are perpendicularly illuminated by a narrow column of photons (simulating a well collimated beam). The stochastic nature of the model relies on random sampling of variables from probability distributions. The modern sampling algorithms of modern commercial computers prove capable of generating uniformly distributing random variables, which are employed here.

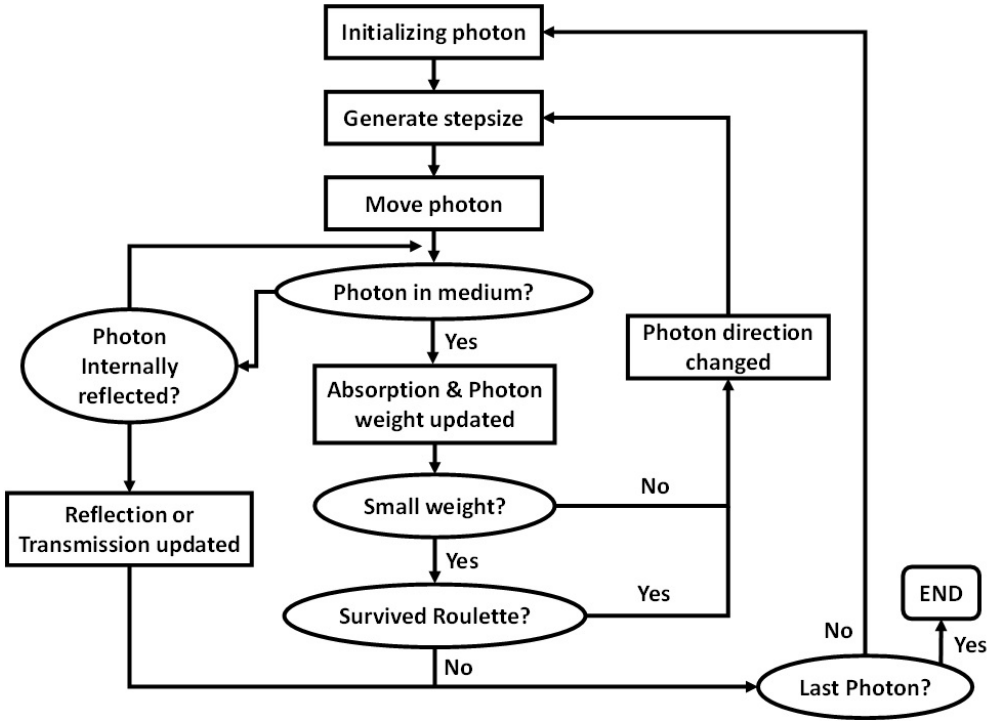

Figure 5.2: A A flow diagram explaining the key aspects of a Monte-Carlo simulation of photon propagation in turbid media.

5.1.1 Photon Launch

All launched photon are initially assigned a weight of unity ($W = 1$). If a mismatch in boundaries at the surface of the tissue exists, specular reflectance (R_{sp}) will occur. This can be expressed functionally as,

$$R_{sp} = \frac{(n_i - n_t)^2}{(n_i + n_t)^2} \tag{5.1}$$

where n_t and n_i are the ambient and sample refractive indices, respectively. In the model, the affects of specular reflection to a propagating photon is reflected as decrement to the overall photon weight ($W = 1 - R_{sp}$).

5.1.2 Photon Stepsize

The stepsize of the propagating photon (s) can be calculated based on a random sampling of the probability density for s. By randomly generating a variable ζ between the intervals $(0, 1]$, the stepsize can be fictionalized as (eq. 5.2),

$$s = \frac{-\ln \zeta}{\mu_t} \tag{5.2}$$

where $\mu_t = \mu_s + \mu_a$ with units of cm^{-1}. As described in section 1.2, the inverse of the total attenuation (μ_t) describes the mean free path between photon-tissue interactions. For typical biological tissues, the total scattering values can be two orders of magnitude greater than the absorption values [1, 15].

5.1.3 Photon Movement

By registering a photon's initial position ($\vec{s_0} = (x, y, z)$) and with the stepsize (s) estimated, a photon can be moved within the tissue. The trajectory of this photon is specified by a unit vector ($\vec{s}$), which is characterized by directional cosines (μ_x, μ_y, μ_z). Incorporating these trajectories, the position of the photon can be updated as follows,

$$\vec{s'} = \vec{s_0} + \vec{s}\,s \tag{5.3}$$

$$x' = x + \mu_x s \qquad y' = y + \mu_y s \qquad z' = z + \mu_z s \tag{5.4}$$

5.1.4 Photon-Tissue Interaction: Absorption

As the photon propagates in the tissue, some attenuation of the photon occurs as absorption by the tissue. This is reflected in the weight as a change to the overall weight of the photon (W),

$$W' = W - \left(\frac{\mu_a}{\mu_t}\right)W \tag{5.5}$$

This photon, with its new weight can now undergo scattering by the tissue.

5.1.5 Photon-Tissue Interaction: Scattering

To simulate the scattering of a photon by the tissue, a deflection angle ($0 \leq \theta < \pi$) and azimuthal angle ($0 < \psi < 2\pi$) are statistically sampled. A described in section 1.3.1, the probability distribution for the cosine of the deflection angle can be described by the Henyey-Greenstein function. Random values for $cos\theta$ can be generated, and hence equation 1.4 can be written as,

$$\begin{aligned} cos\theta &= \frac{1}{2g}\left\{1+g^2\left[\frac{1-g^2}{1-g+2g\zeta}\right]^2\right\} \qquad \text{if} \quad g \neq 0 \\ &= 2\zeta - 1 \qquad\qquad\qquad\qquad\qquad\quad \text{if} \quad g = 0 \end{aligned} \tag{5.6}$$

Similarly, the azimuthal angle can be expressed as a random number distributed over the ranges of 0 to 2π as $\psi = 2\pi\zeta$. With the deflection and azimuthal angles defined, the new directional cosines of the simulated photon can now be calculated as,

$$\begin{aligned} \mu_x' &= \frac{\sin\theta}{\sqrt{1-\mu_z^2}}(\mu_x\mu_z\cos\psi - \mu_y\sin\psi) + \mu_x\cos\theta \\ \mu_y' &= \frac{\sin\theta}{\sqrt{1-\mu_z^2}}(\mu_y\mu_z\cos\psi - \mu_x\sin\psi) + \mu_y\cos\theta \\ \mu_z' &= -\sin\theta\cos\psi\sqrt{1-\mu_z^2} + \mu_z\cos\theta \end{aligned} \tag{5.7}$$

If the photon's direction of propagation is substantially close to the z axis (quantified as $|\mu_z| > 0.99999$), equations 5.7 can be transformed as follows so as to avoid divisions by a small number,

$$\mu_x' = \sin\theta\cos\psi \quad \mu_y' = \sin\theta\sin\psi \quad \mu_z' = \text{SIGN}(\mu_z)\cos\theta \tag{5.8}$$

where SIGN(μ_z) return 1 when μ_z is positive and returns -1 when μ_z is negative.

5.1.6 Photon-Tissue Interaction: Boundaries

As the photon propagates within the tissue, it may hit the boundary between the tissue and the ambient medium. Due to the infinitely thin geometry of the modelled sample, the tissue boundaries exist across the z axis - at $z = 0$ and $z = \tau$, where τ is the sample thickness. By monitoring the photon's new position across the z axis (i.e. $z' \leq 0$ and $z' \geq \tau$), one can conclude if the photon has hit the boundaries of the tissue. One of two things can happen to the photon at this interface - either it is internally reflected or transmitted across the boundary. Photon propagation continues if it is internally reflected back into the tissue, but ceases simulations if the photon crosses the boundary into the ambient medium. Depending on which direction the photon escapes the tissue, it is accounted as reflectance or transmittance. The following steps will be employed to accurately simulate these photon-boundary interactions,

- **Step 1:** To determine if the photon will escape the tissue-ambient medium boundary or if it will be internally reflected.

If the photon is incident on either boundary of the sample, the probability of the photon to be internally reflected is dependent on the angle of incidence ($\theta_i = \cos^{-1}(|\mu_z|)$). Corresponding to the boundary in the direction of propagation of the simulated photon, the value of θ_i can be calculated as follows,

$$\begin{aligned} \theta_i &= \cos^{-1}(\mu_z) \qquad \text{if} \quad \mu_z \geq 0 \\ &= \pi - \cos^{-1}(\mu_z) \qquad \text{if} \quad \mu_z < 0 \end{aligned} \tag{5.9}$$

Snell's law provides a relationship between the angle of incidence and angle of transmittance at an interface of two media of different refractive indices ($n_i \sin\theta_i = n_t \sin\theta_t$). The internal reflectance ($R(\theta_i)$) is set to 1, if θ_i is larger than the critical angle. In all other cases, $R(\theta_i)$ can be calculated using Fresnel's formulas,

$$R(\theta_i) = \frac{1}{2}\left[\frac{\sin^2(\theta_i - \theta_t)}{\sin^2(\theta_i + \theta_t)} + \frac{\tan^2(\theta_i - \theta_t)}{\tan^2(\theta_i + \theta_t)}\right] \tag{5.10}$$

which is an average of the reflectances for the both polarizations as the simulated photons are independent of either orthogonal polarization of incident light.

- **Step 2:** Photon moved to the incident boundary.

As mentioned above, the photon has now crossed one of the two boundaries of the tissue (i.e. $z' \leq 0$ and $z' \geq \tau$). To move the photon to the boundary of the tissue, a fraction of the stepsize is taken by

the photon. Based on this foreshortened stepsize (s') the position of escape of the photon (x', y') is calculated by substituting s' as s in equations 5.4.

$$\begin{aligned} s' &= \frac{-z}{\mu_z} \qquad \text{if} \quad \mu_z \leq 0 \\ &= \frac{\tau - z}{\mu_z} \qquad \text{if} \quad \mu_z \geq \tau \end{aligned} \tag{5.11}$$

- **Step 3:** Depending on photon reflection or transmission at the boundary, the photon trajectories or the reflectance and transmittance arrays are updated respectively.

If the photon successfully propagates over the boundary between the tissue and the ambient medium, the photon contributes to reemittance. Depending on which surface the photon exits the tissue, the weights are recorded into a reflectance or transmittance array.

$$\begin{aligned} R_d(x', y') &= R_d(x', y') + W \\ T_t(x', y') &= T_t(x', y') + W \end{aligned} \tag{5.12}$$

If the photon is reflected back into the tissue, a fraction of the photon weight escapes the media as observable energy distribution and is stored in the generated reflectance array (eq. 5.13). This is followed by a new weight calculated for the photon ($W \leftarrow R(\theta_i)W$).

$$\begin{aligned} R_d(x', y') &= R_d(x', y') + (1 - R(\theta_i))W \\ T_t(x', y') &= T_t(x', y') + (1 - R(\theta_i))W \end{aligned} \tag{5.13}$$

Due to the internal reflection of the photon, its trajectory and position inside the tissue is updated. The x and y coordinates of the photon can be computed using the full length of s while the the z coordinate can be changed as described using equations 5.14. Correspondingly, the directional cosine in the z coordinate is updated as well ($\mu_z \leftarrow -\mu_z$).

$$\begin{aligned} z &\leftarrow -z \qquad \text{if} \quad z \leq 0 \\ z &\leftarrow 2\tau - z \quad \text{if} \quad z \geq \tau \end{aligned} \tag{5.14}$$

5.1.7 Photon Termination

If the photon has remitted from the modelled medium, it is automatically terminated. Alternatively, if the photon has undergone multiple interactions with the tissue, the weight of the photon will be sufficiently decreased and the photon itself will yield little useful information. Hence, photons

must be properly terminated so as to ensure conservation of energy. This is achieved by a technique called *Russian roulette*, that terminates a photon when the weight falls below a threshold ($W_{th} < 0.0001$). The method gives the photon one in m chances of surviving with a weight of mW. This is mathematically summarized below (eq. 5.15),

$$\begin{aligned} W \leftarrow \quad mW \qquad & \text{if} \qquad \xi \leq \frac{1}{m} \\ 0 \qquad & \text{if} \qquad \xi > \frac{1}{m} \end{aligned} \tag{5.15}$$

where ξ is a uniformly distributed pseudorandom number such that $0 \leq \xi \leq 1$. Hence, this method terminates photons in an unbiased manner while the total energy is conserved.

5.1.8 Photon Distribution at Launch

For the purposes of the simulation, we assume our modelled samples to be illuminated by a flat-beam of radius w. We set the energy of this beam to be of arbitrary units (1 unit $\approx$ 1 J). Due to the steady-state nature of the Monte-Carlo simulations, the energy and power can be easily converted. The radiant exposure of the source can be functionally represented using equation 5.16,

$$\begin{aligned} S(r) &= \frac{1}{\pi w^2} \qquad \text{if} \quad r \leq w \\ &= 0 \qquad\quad \text{if} \quad r > w \end{aligned} \tag{5.16}$$

However, the probability density function ($p(r)$) must be normalizable for a radial distribution ($\int_0^w p(r)dr = \int_0^w S(r)2\pi r dr = 1$). Through the normalization process, an expression for the probability density function can be obtained ($p(r) = 2r/w^2$). To randomly choose an appropriate position to launch a photon within the radius of the modelled beam, a random number (ζ) within the interval [0, 1] is applied.

$$\zeta = \int_0^r p(r)dr = \int_0^r \frac{2r}{w^2}dr = \frac{r^2}{w^2} \Rightarrow r = w\sqrt{\zeta} \tag{5.17}$$

Due to the cylindrical symmetry of the problem around the z axis, the photon deposition can be stored in a simple 2-D array and photon launch may simply occur at $x = w\sqrt{\zeta}$ and $y = 0$ with a trajectory normal to the surface of the tissue ($\mu_x = 0, \mu_y = 0, \mu_y = 1$) (eq. 5.17).

5.2 Finite Volume Modelling

Since the goal of this thesis is to model the light losses observed in the IS measurements of turbid samples (summarized in chapter 4), the Monte-Carlo model described above can be implemented to model the light propagation through a sample with finite dimensions. This developed MC model of finite samples will be referred as "finite-MC" for the remainder of this thesis. The sample is visualized as a finite slab with a defined thickness (τ) described with boundaries, $z = 0$ and $z = \tau$. The lateral dimensions (across the x and y axes) of the slab are described with boundaries, x_{right}, x_{left}, y_{front} and y_{back} (as described in figure 5.3). The steps described in section 5.1.6 can be updated to incorporate the four other possible boundaries of exit.

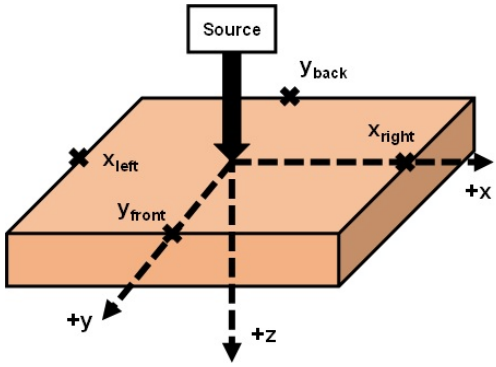

Figure 5.3: A geometry of a sample modelled by the Finite Monte-Carlo model. The four boundaries of the sample are described by the parameters, x_{right}, x_{left}, y_{front} and y_{back}

- **Updated step 1:** Determining if the photon will escape or be internally reflected.

Due to the presence of four other boundaries, the angle of incidence can be determined using the two other directional cosines as follows,

$$\theta_i = \begin{cases} cos^{-1}(\mu_z) & \text{if} \quad \mu_z \geq 0 \\ \pi - cos^{-1}(\mu_z) & \text{if} \quad \mu_z < 0 \\ cos^{-1}(\mu_y) & \text{if} \quad \mu_y \geq 0 \\ \pi - cos^{-1}(\mu_y) & \text{if} \quad \mu_y < 0 \\ cos^{-1}(\mu_x) & \text{if} \quad \mu_x \geq 0 \\ \pi - cos^{-1}(\mu_x) & \text{if} \quad \mu_x < 0 \end{cases} \tag{5.18}$$

using the new computed angle of incidence from equations 5.18, a decision on whether the photon is internally reflected or crosses the boundary can be made as described in section 5.1.6.

- **Updated step 2:** Photon moved to the nearest incident boundary.

In contrast to the two boundary model, the fraction of the stepsize taken by the photon depending on which one of the four surfaces it exits is described as follows,

$$s' = \begin{cases} = \dfrac{-z}{\mu_z} & \text{if} \quad \mu_z \leq 0 \\ = \dfrac{\tau - z}{\mu_z} & \text{if} \quad \mu_z \geq \tau \\ = \dfrac{-x_{left} - x}{\mu_x} & \text{if} \quad \mu_x \leq -x_{left} \\ = \dfrac{x_{right} - x}{\mu_x} & \text{if} \quad \mu_x \geq x_{right} \\ = \dfrac{-y_{back} - y}{\mu_y} & \text{if} \quad \mu_y \leq -y_{back} \\ = \dfrac{y_{front} - y}{\mu_y} & \text{if} \quad \mu_y \geq y_{front} \end{cases} \tag{5.19}$$

where τ is the thickness of the sample and x_{right}, x_{left}, y_{front} and y_{back} are the positions of the lateral boundaries of the modelled sample (as described in fig. 5.3). This shortened stepsize will be moved to the boundary and its positions updated correspondingly.

- **Updated step 3:** Photon updated as light escaped as fluence from respective surface.

Similar to step 3 in section 5.1.6, four other arrays corresponding to the lateral surface of exit to record the weights of the exiting photon will be created. Internal reflection changes the coordinates of the photon depending on corresponding surface of incidence. For example, similar to the boundaries along the z-axis, if the photon is incident on either boundary across the x axis, the z and y coordinates of the photon can be computed using the full length of the step (s) while the x position can be updated as described,

$$x' \leftarrow \begin{cases} = x_{right} - \mu_x(s - s') & \text{if} \quad \mu_x \geq x_{right} \\ = -x_{left} - \mu_x(s - s') & \text{if} \quad \mu_x \leq x_{left} \end{cases} \tag{5.20}$$

5.3 Simulation Results

The traditional MC code is written in the language *C* and is optimized to simulated photon propagation for one set of optical properties. Appendix A.2 describes the structure of the input file required by the finite-MC algorithm. The code has been implemented under MATLAB's environment to streamline simulations of multiple data points (Appendix A.2).

Integrating sphere measurements of total reflectance and transmittance are uniquely depending on a combination of the sample's absorption and scattering. This results in light losses being

uniquely dependent of the sample's optical properties. Hence to analyze the errors across varying combinations of absorption and reduced sacttering values, a 2×2 permutation of two levels of absorption and scattering values. These sets are described in table ,

Sample	LL	LH	HL	HH
$\mu_a\,[cm^{-1}]$	0.04	0.04	4	4
$\mu_s'\,[cm^{-1}]$	3	36	3	36

Table 5.1: Combination of absorption and reduced scattering values used for simulation of light losses in the following sections.

5.3.1 Model Validation

To validate the performance of the developed finite-MC model, its outputs will be compared against the forward adding-doubling (AD) model. Since the AD models samples to be thin infinite slabs, a similar sample geometry can be used to simulate photon propagation using the finite-MC. Hence, for a set of optical properties, the model can be validated. As mentioned in section 5.2, the finite-MC model can run MC simulations for a model with finite geometries. The boundaries of the modelled sample can be defined by providing the appropriate coordinates (i.e. x_{left}, x_{right}, y_{front}, y_{back}). To simulate a thin infinite sample, these parameters can be set to be much greater than the thickness of the sample.

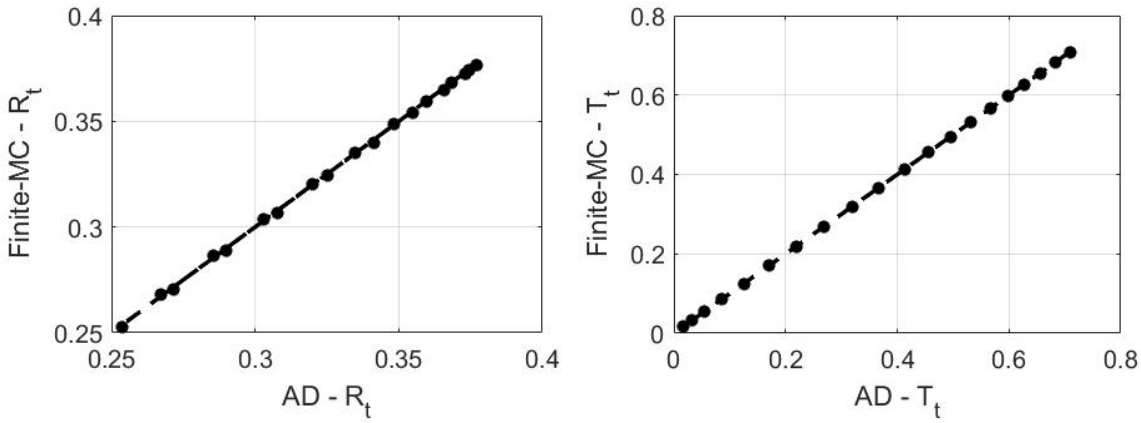

Figure 5.4: Plots compares the total reflectance and transmittance for a set of optical properties of a semi-infinite sample model, simulated using the finite-MC model against the forward AD model.

A semi infinite slab with dimensions $100 \times 100 \times 0.2$ will be simulated to validate the model against the AD model. As described in figure 5.4, the finite-MC predictions of total reflectance and

transmittance match that of the AD calculated values (within relative errors of 0.5 %). The provides confidence in the overall performance of the finite-MC simulations for all sample geometries.

5.3.2 Analysis of Lateral Losses

Lateral light losses refers to photons escaping a sample due to the finite lateral boundaries (described in section 4.19). Theoretically, photons incident closer to the boundaries of the tissue, have a higher probability of escaping out the lateral sides of the modelled sample. To test this in simulation, the light lost through the lateral sides ($L_{sample} = x_{right} - x_{left}$) can be simulated as the diameter of the beam (D_{beam}) used to illuminate the sample, becomes comparable to the side length of the tissue.

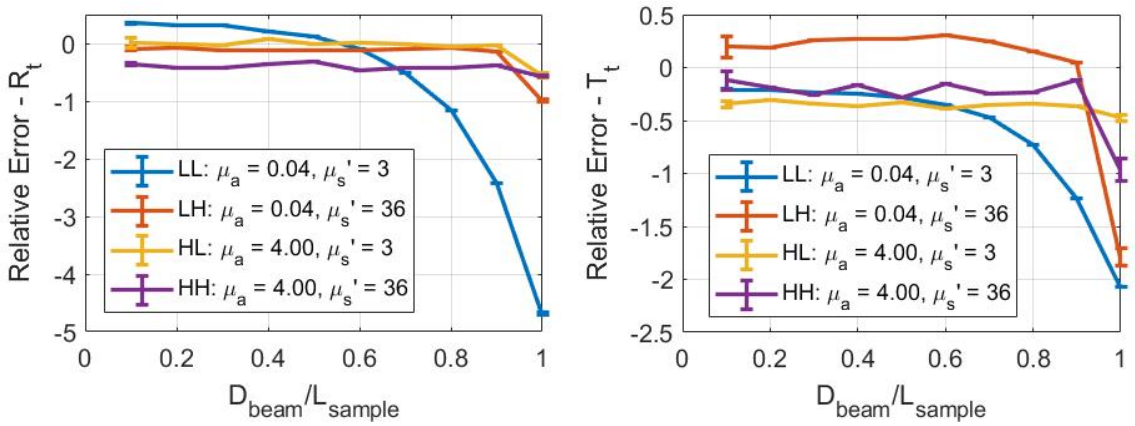

Figure 5.5: Lateral light losses in finite-MC simulated reflectance (left) and transmittance (right) as a function of the ratio between beam diameter (D_{beam}) and sample light (L_{sample}) for the four sets of optical properties. The losses are described in relative errors between finite-MC simulated against AD calculations.

For the four sets of optical properties described in table 5.1, the effects of lateral losses in IS measurements are simulated and described in figure 5.5. As observed, the highest losses (up to 2 %) are seen for most optical property sets when the beam diameter becomes significantly comparable to the size of the port (i.e., $>$ 80 %). The most significant losses are observed for the combination of low absorption and scattering samples (up to 5 %). The losses for this range of optical properties can be observed for beam diameters greater than 50 % the sample length. The simulated photon energy distribution out of the finite-MC model can be translated into optical properties and compared to those mentioned in the table 5.1.

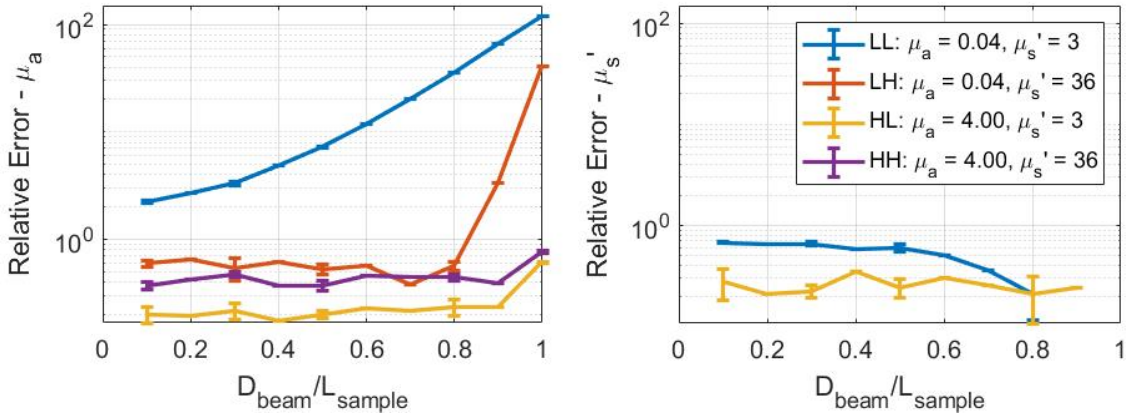

Figure 5.6: Effects of lateral light losses in IAD estimated absorption (left) and reduced scattering (right) values as a function of the ratio between beam diameter (D_{beam}) and sample light (L_{sample}) for the four sets of optical properties. The losses are described in relative errors between IAD calculated against "true" optical properties.

Figures 5.6 describe the relative errors in IAD calculated optical properties from outputs obtained from finite-MC simulations. The lateral losses in IS measurements have little to no effect on IAD estimated scattering values. However, significant errors in IAD estimated absorption values arise due to these losses for the lower absorption values (up to a 100 %). Due to the observations seen in figures 5.5, the high errors in absorption can be attributed to the significant deviation of the simulated reflectance due to these lateral losses.

5.3.3 Analysis of hemispherical losses

Hemispherical light losses refer to photons escaping the collection area of the IS sample port as it re-emerges out a illuminated sample. Similar to lateral losses, we theorize hemispherical losses to be significant as the illumination beam diameter becomes significant to the diameter of the IS sample port. This can be tested in simulation, by varying the beam diameter (D_{beam}) with respect to IS sample port (D_{sample}), the losses in the hemispherical light losses experienced by IS measurements can be quantified.

Figure 4.20, describes the effects of hemispherical losses in IS measurements through finite-MC simulations. As observed, the highest losses in both reflectance and transmittance measurements correspond to the low absorbing and low scattering set at all beam to port diameter ratios (up to 25 %). For the other sets of optical properties, maximum errors of up to 5 % are observed when the illumination beam diameter is significantly comparable to the port diameter (> 80 %). It must be

noted that the effects of the hemispherical losses are more significant to reflectance measurements than transmittance values.

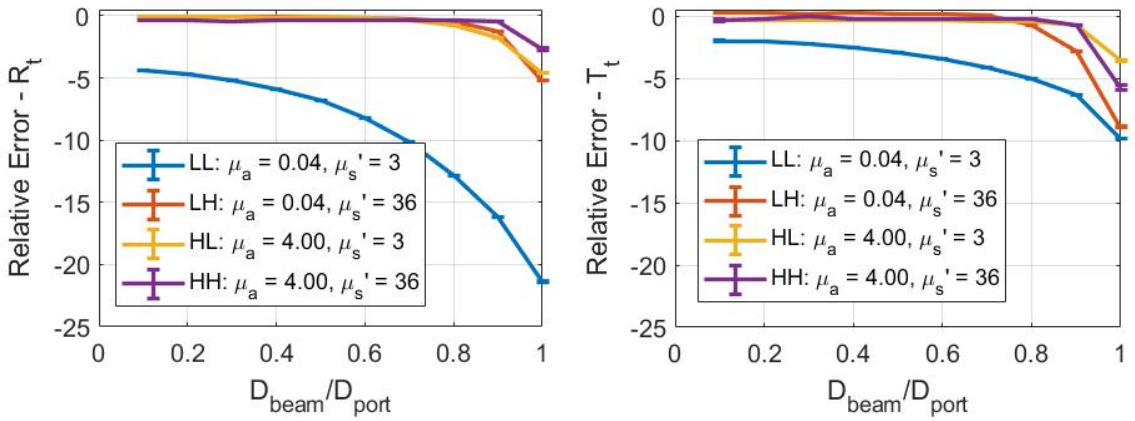

Figure 5.7: Hemispherical light losses in finite-MC simulated reflectance (left) and transmittance (right) as a function of the ratio between beam diameter (D_{beam}) and IS sample port diameter (D_{port}) for the four sets of optical properties. The losses are described in relative errors between finite-MC simulated against AD calculations.

By calculating the optical properties using the IAD from the set of reflectance and transmittance values simulated by the finite-MC model, the effects of hemispherical losses on these estimations can be quantifies. As observed in figure 5.8-left, hemispherical losses significantly affect the estimations of low absorption coefficients. It must be noted for samples with low absorption and scattering values, the effects of hemispherical losses will be present at all beam and port configurations. The low absorption values are commensurate to those water, and hence these ranges will be avoided in future analyses. A beam diameter much smaller than 40 % the size of the sphere port must be ensured when measuring low absorption and high scattering samples. When observing scattering estimations, it must be noted that the maximum errors faced are only up to 5 %. Generally, the scattering measurements can be made accurate with a beam diameter less than 80 %.

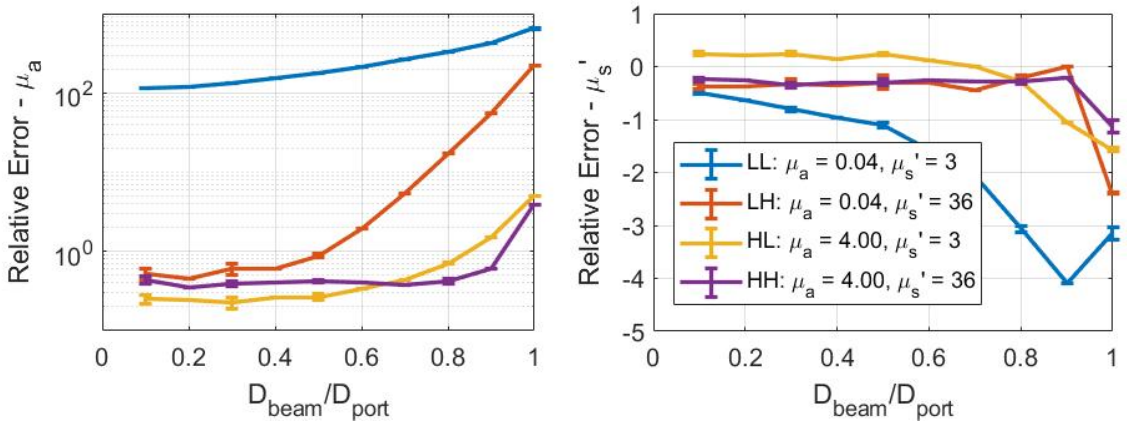

Figure 5.8: Effects of hemispherical light losses in IAD estimated absorption (left) and reduced scattering (right) values as a function of the ratio between beam diameter (D_{beam}) and the diameter of the IS sample port (D_{port}) for the four sets of optical properties. The losses are described in relative errors between IAD calculated against ”true” optical properties.

Chapter 6

Integrating Sphere Corrections

Integrating sphere measurements made on samples illuminated by a beam whose diameter is either comparable to the sample dimensions or the sample port of the IS, light losses in the form of hemispherical and later losses (as described in chapter 4). In chapter 5, we explored these losses using the finite-MC model and observed that hemispherical losses affect IS measurements greater than lateral losses, with up to 25 % relative errors in measurements. These high errors were observed for lower absorption and scattering samples ($\approx 0.04\,cm^{-1}$ and $3\,cm^{-1}$). Hence, for the dataset II described in chapter 4, inverse calculations of absorption coefficients will be omitted due the true values falling below these thresholds. Through the results of the simulations, it was observed that the light losses were predominant for samples illuminated by beam diameters greater than 80 % the side length of the sample or the IS port diameter. The halogen source used to illuminate the samples in the preliminary tests, has a wide beam diameter of $20\,mm$ which when compared with the IS port and sample sizes have ratios of up to 80 % and 40 %, respectively. In simulation, we observed that if the beam used to illuminate the sample is less than 50 % the sample side length and the IS port radius, the losses described in chapter 4. In practice, this can be implemented experimentally by using a highly contained and well collimated broadband laser. such as a supercontinuum source whose beam diameter is $1.5\,mm$ will be used. This beam diameter is 3 % and 6 % of the sample side and port diameter, respectively.

The preliminary datasets I & II described in chapter 4, can be measured using an integrating sphere with the supercontinuum laser as the source of illumination. The measured quantities can be given to the IAD to estimate optical properties and compared with the analyses done in chapter 4.

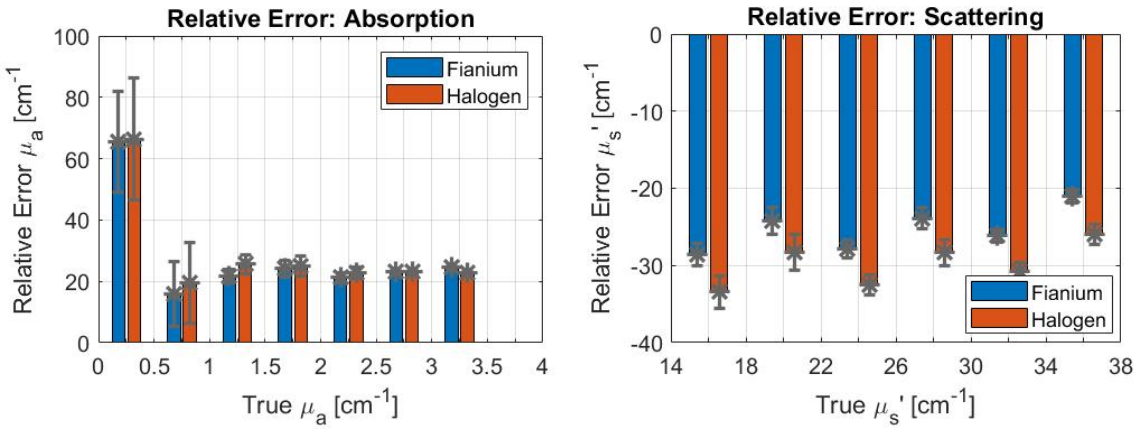

Figure 6.1: Comparison of relative errors in IAD estimated absorption (left) and scattering (right) between IS measurements made using Fianium (blue bars) and Halogen (orange bars) sources of Dataset I.

Figure 6.1 describes the relative errors in the IAD estimated optical properties of the samples illuminated by the fianium and halogen sources. It must be noted that, though incorporating the supercontinuum source reduces the relative errors in the inverse calculations, predominant errors still persist in both calculated optical properties. The greatest reduction in error due to the incorporation of the Fianium source is observed in the calculations of scattering over absorption. When observing the performance of the two sources at lower scattering values (by extending to dataset II), we observe that these errors slightly increase with the highest errors ($\approx 40\,\%$) at reduced scattering values in the range of $0-3\,cm^{-1}$ (Fig. 6.2).

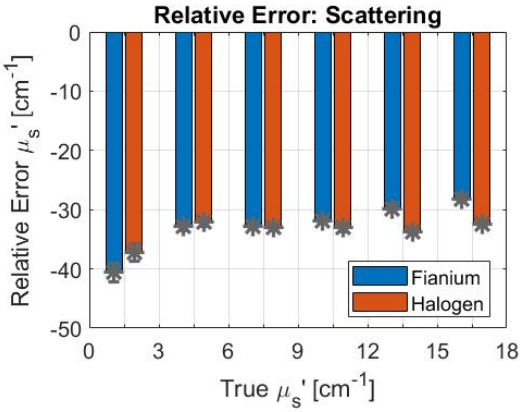

Figure 6.2: Comparison of relative errors in IAD estimated scattering (right) between IS measurements made using Fianium (blue bars) and Halogen (orange bars) sources of Dataset II.

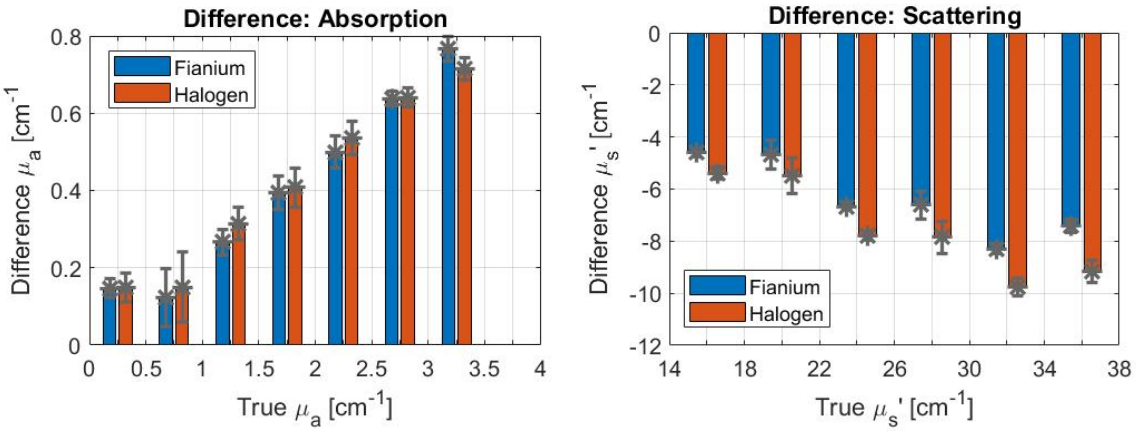

Figure 6.3: Comparison of difference in IAD estimated absorption (left) and scattering (right) between IS measurements and true values, made using Fianium (blue bars) and Halogen (orange bars) sources.

When observing the differences between the absorption and scattering values against true optical properties, it can be observed that estimates from fianium measurements perform better (similar to above). Incorporation of the more finely collimated source improved the resolution of the system, though slightly, in the estimation of optical properties, with the greatest improvement (of $\approx 1.5\,cm^{-1}$) to the scattering estimates. Similarly, the average resolution in absorption estimations have also improved by $\approx 0.015\,cm^{-1}$. It must be noted that these differences increase with the optical properties of the sample, with the lowest differences being $0.14\,cm^{-1}$ in calculated absorption and $1.4\,cm^{-1}$ in reduced scattering values.

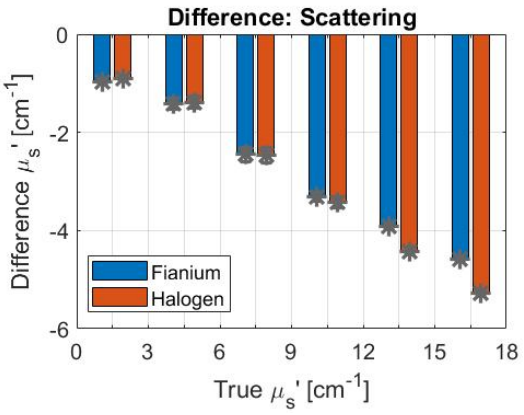

Figure 6.4: Comparison of difference in IAD estimated scattering (right) between IS measurements made using Fianium (blue bars) and Halogen (orange bars) sources of Dataset II.

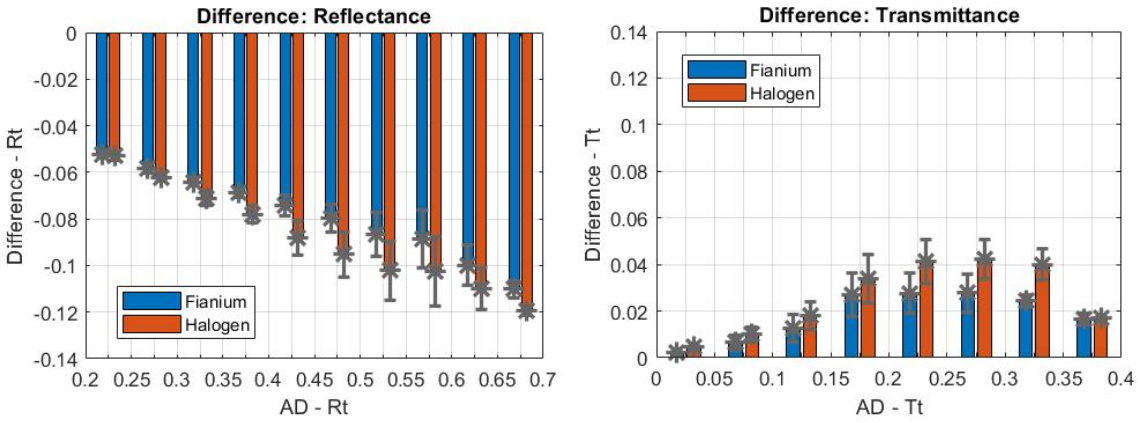

Figure 6.5: Comparison of differences in IS measured reflectance (left) and transmittance (right) against AD predicted values of samples illuminated using Fianium (blue bars) and Halogen (orange bars) sources, for dataset I.

When observing the raw measurements of reflectance and transmittance made using the IS and the two sources, halogen and fianium, we observe fianium measurements to be closer to the expected measurements derived from AD calculations, overall (Fig. 6.5). In reflectance measurements, the lowest resolution of the IS is ≈ 0.05 which correspond to the lower reflectance values. Conversely, for higher reflectance values, the resolution increases up to 0.12. The average resolution for these ranges for the halogen and fianium sources are 0.08 and 0.09, respectively. On the other hand, the IS measurements of transmittance have more contained resolutions with the lowest being 0.001 and highest being 0.05. The resolution for transmittance measurements average to 0.02 and 0.03 for the fianium and halogen soruces, respectively.

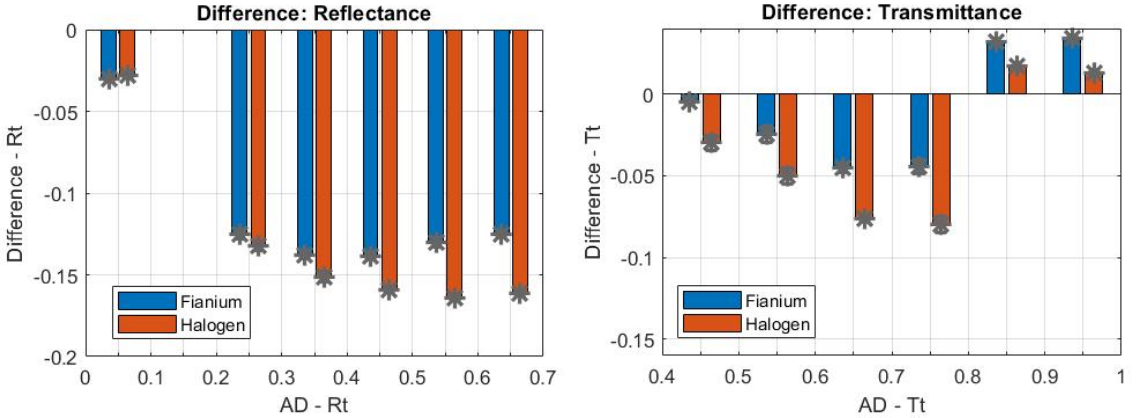

Figure 6.6: Comparison of differences in IS measured reflectance (left) and transmittance (right) against AD predicted values of samples illuminated using Fianium (blue bars) and Halogen (orange bars) sources, for dataset II.

Due to the varies range of optical properties of dataset II, lower and higher ranges of reflectance

and transmittance values, respectively, are measurement with the IS (Fig. 6.6). Consistent with the observations for dataset I, the differences in measurements are lower for transmittance than reflectance measurements. Overall, the fianium measurements are better than those made with the halogen source. However, this behavior deviates at the extremes of these measurement ranges.

To summarize the observations described above, incorporation of a supercontinnum source, a highly collimated broadband laser, has not eliminated the errors in IS measurements, that were observed in measurements made using a halogen source (chapter 4). However, the fianium source was able to reduce the resolution of the IS measurements than the halogen source, with the greatest improvements being for measurments within the ranges of $0.5 - 0.7$. We can conclude that the errors in IS measurements are greater than the influences of lateral and hemispherical light losses.

The errors that persist in these IS measurements can be attributed to the response of the IS to the presence of the sample mounted onto the IS port. As described in chapter 2, the IS is an optical resonator where a given measurement is a result of the multiple internal reflections of light collected by the device. However, when the standard is substituted with the sample, the total power collected by the device drops considerably. This loss in total power collected is often described as the substitution error [33, 34, 37]. In this chapter, we will explore the various correction schemes commonly used to eliminate the losses in IS measurements due to the substitution error.

6.1 Experimental correction

Characterization of the effects of the substitution error on IS measurements can be performed experimentally, by ensuring that the total fluence collected by the system is devoid of losses once the sample is mounted onto the sphere. Two common methods to ensure this has been described - incorporation a double beam configuration or an addition measurement through diffuse illumination of the sample. The former has multiple disadvantages, from a much more complex setup and inflexibility to rotate the sphere due to complications

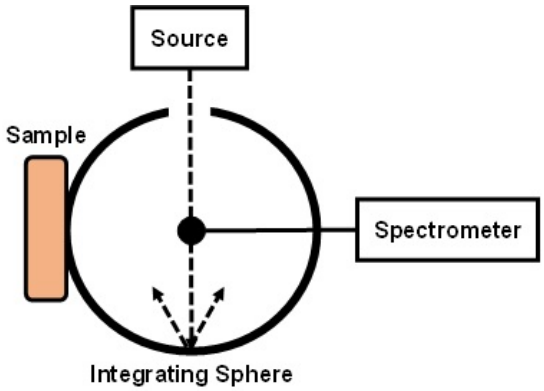

Figure 6.7: A schematic describing the top-to-bottom view of the IS configuration for making measurements of R_{diff} for a given sample.

in geometry [17, 31]. The later provides flexibility to adjust the experimental configuration, but increases the total time to complete all measurements for a given sample. Here, the incorporation of the diffuse illumination of the sample will be explored as an experimental collection for the substitution error.

From the results summarized in chapter 4, the substitution error affects measurements of total reflectance more significantly than total transmittance. Hence, for the following correction scheme will only be implemented for measurements of total reflectance. As mentioned in chapter 2, equations 2.1 are used to calculate the total reflectance and transmittance for a sample. An addition measurement of the sample with a diffuse illumination will be taken. The diffuse illumination can be achieved by focusing the illumination beam to be incident on the sphere wall over the sample as typically done (described in figure 6.7). The signals measured this way, will be referred to as R_{diff}. Now the measurements of total reflectance measurement can be corrected (R_T^C) by updating equation 2.1, using the R_{diff} measurement as,

$$R_T^C = \frac{R_{sample} - R_{dark}}{R_{diff} - R_{dark}} \tag{6.1}$$

For the dataset I described in this thesis, a corrected reflectance value using equation 6.1, will be employed. The effects of this correction on the raw reflectance values and the inverse calculations of optical properties, will be explored in the following sections.

6.1.1 Analysis of measurements

The effect of the experimental correction scheme of total reflectance measurements can be quantified through comparisons from calculations using the forward model (AD) (similar to above). Here, the effects of the correction for both sources - fianium and halogen for samples in dataset I will be contrasted.

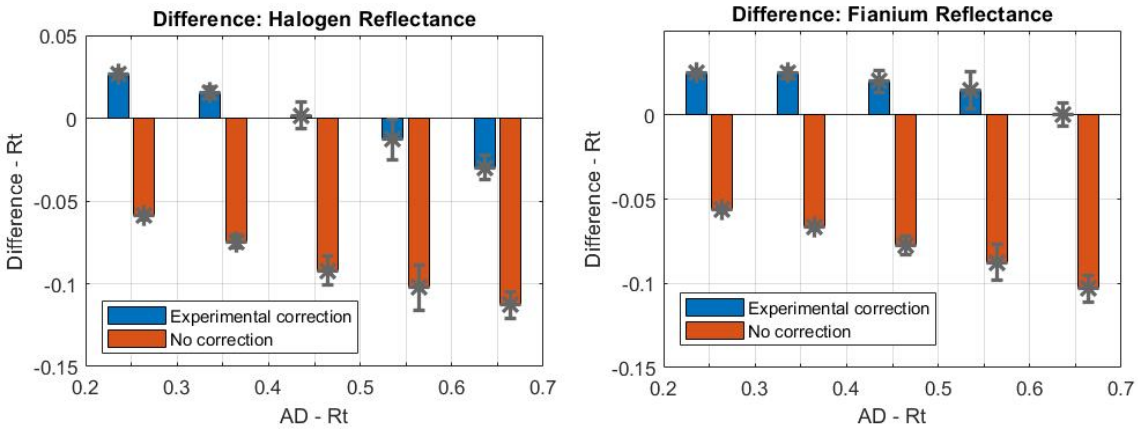

Figure 6.8: Differences of total reflectance values against AD calculations for experimental correction (blue bars) and raw IS measurements with no corrections (orange bar) for dataset I samples illuminated using fianium (right) and halogen (left) source.

Figure 6.8, compares differences between corrected reflectance values and forward AD calculations against those differences with no correction employed to the reflectance measurements, for measurements taken with the halogen and fianium sources. As observed, implementation of the experimental correction significantly improves overall reflectance values of all samples, regardless of source. With implementation of this correction method, the overall resolution of reflectance measurements have decreased to 0.017 for both sources.

6.1.2 Analysis of inverse calculations

Optical properties for the set of corrected reflectance values can be calculated using the IAD. The effects of incorporating this correction scheme to the inverse calculations of optical properties can be quantified by comparing with true optical properties of samples.

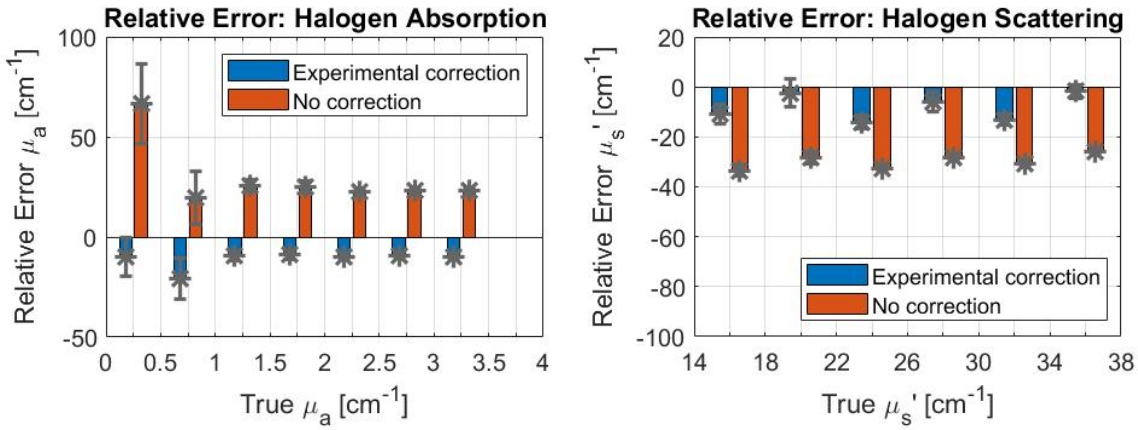

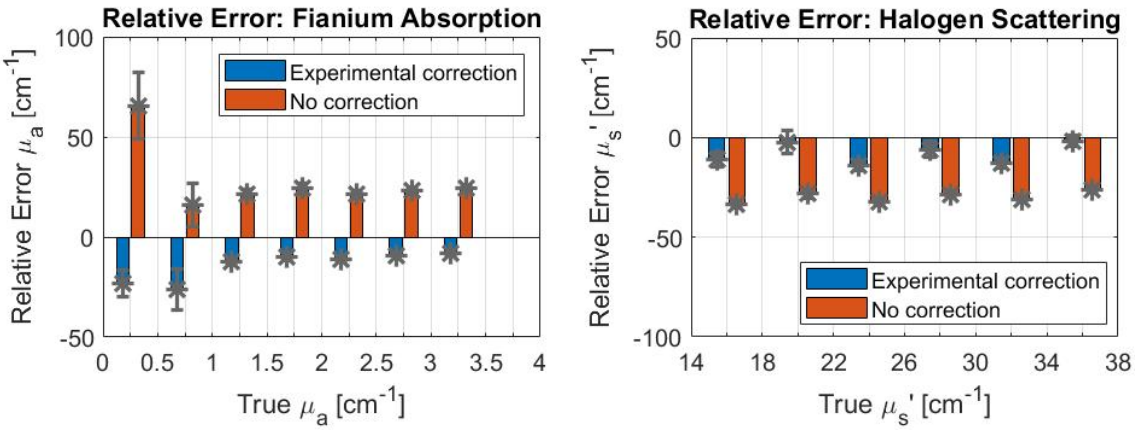

Figure 6.9: comparison of relative errors in IAD estimated absorption (left) and reduced scattering (right) values for experimental correction versus no correction, for measurements taken with Fianium (below) and Halogen (above) sources.

When observing the relative errors in the estimations of optical properties with incorporation of the experimental correction, an overall improvement can be observed (Fig. 6.9). Relative errors in inverse estimations of absorption coefficients have decreased for the halogen (mean errors 11 %) greater than that with the fianium (mean errors 14 %) source with incorporation of the experimental correction. On the other hand, inverse estimations of scattering have improved for the fianium (mean errors 3 %) source over the halogen (mean errors 8 %) source with the addition of experimental corrections to reflectance measurements.

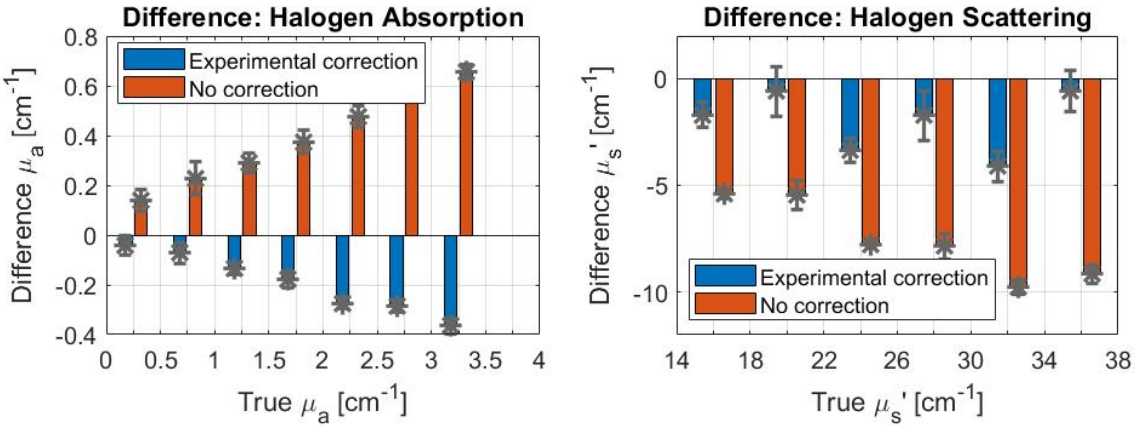

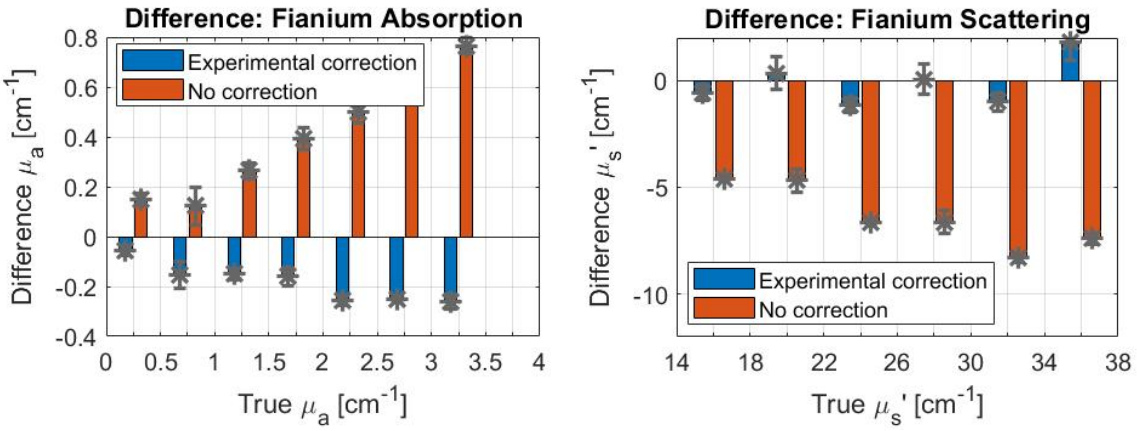

Figure 6.10: comparison of differences in IAD estimated absorption (left) and reduced scattering (right) values against true properties for measurements taken with experimental correction and no correction. The effects on these differences for both sources - Fianium (below) and Halogen (above) are described.

Incorporation of the experimental correction has improved the overall resolution of the IS/IAD method to estimate optical properties (Fig. 6.10). For the halogen source, the mean resolution of inverse calculated absorption and reduced scattering have decreased to $0.17\,cm^{-1}$ and $2\,cm^{-1}$, respectively. Conversely, for the measurements taken with the fianium source, the resolutions of the system for inverse calculated absorption and reduced scattering have decreased to $0.185\,cm^{-1}$ and $0.8\,cm^{-1}$, respectively. As described above, the incorporation of the experimental correction improves overall resolution of the IS/IAD method to retrieve optical properties with significant improvement of the inverse calculation of reduced scattering values from fianium measurements.

6.2 Theoretical correction

The integrating sphere is an optical resonator, were measured values are dependent on the multiple reflection within the internal surface of the IS. Multiple reflections falling on non-white areas in the sphere (e.g. sample, detector, and entrance), will decrease the total power collected by the system. In the previous section, this loss in power was corrected using an additional measurement to increase the total power collected by the system. However, the total power collected by the IS can be described as a function of the geometric and reflection parameters of the sphere (as described in section 2.1.1). If these sphere parameters are known, the loss of power in the IS measurements can be accounted. The IAD provides such an option such that the inverse calculations of optical properties can be improved by theoretically correcting the input IS measurements [32]. Furthermore, *Prahl et. al.* has incorporated a hybrid IAD-MC approach to correct for light losses observed due

to the finiteness of the sample and IS port with respect to beam diameter (as described in chapter 4). Here, the MC program is used to estimate the amount of light lost for a given set of optical properties. The lost light is then incorporated back into the next iteration of the IAD to estimate optical properties.

6.2.1 Analysis of inverse calculations

As described above, the IAD can be set to estimate optical properties while incorporating the theoretical correction to the input IS measurements. Here, the effects of including this correction to inverse estimations of optical properties will be analyzed.

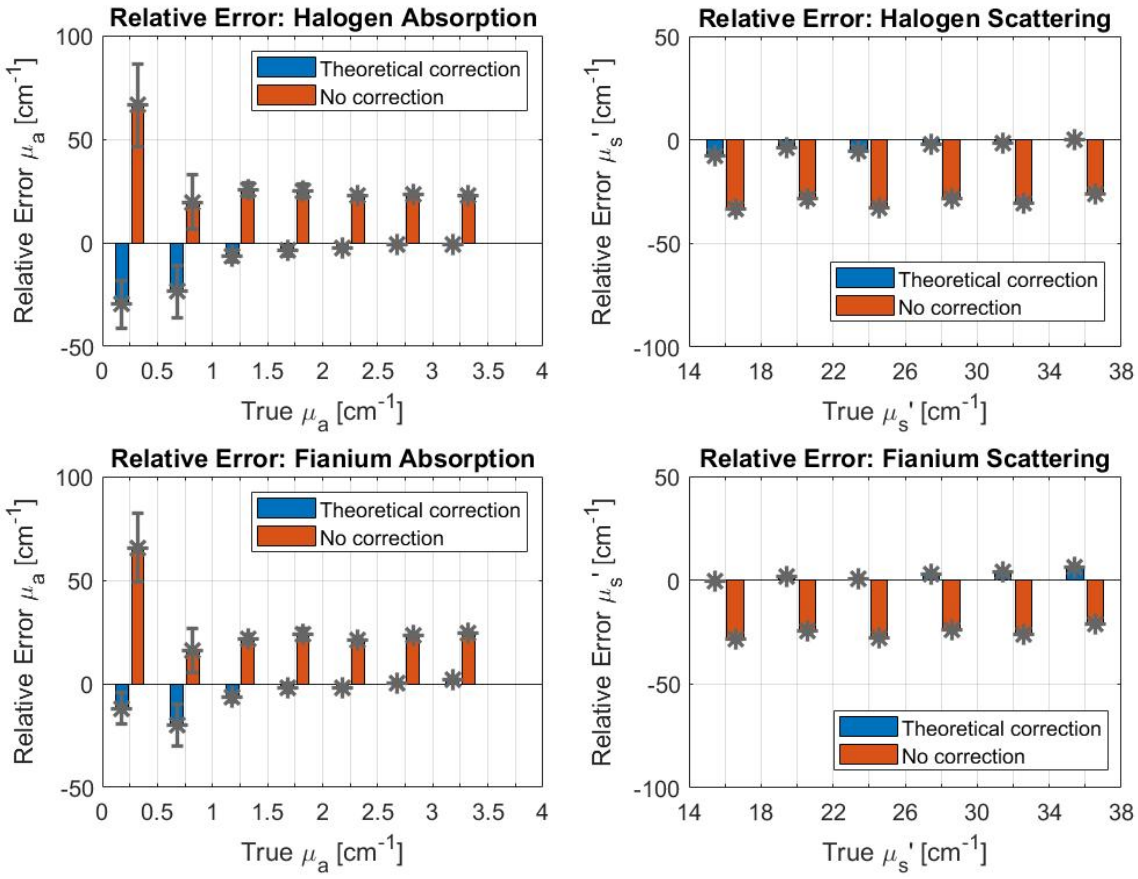

Figure 6.11: comparison of relative errors in IAD estimated absorption (left) and reduced scattering (right) values for theoretical correction versus no correction, for measurements taken with Fianium (below) and Halogen (above) sources.

Trends in relative errors in the estimation of optical properties with incorporation of the theoretical correction evidently describes significant improvements to the accuracy of the inverse calculations

(Fig. 6.11). Relative errors in inverse calculations of absorption have decreased to 9.6 % and 6.4 % for the halogen and fianium sources, respectively. Similarly, inverse calculations of scattering has improved to relative errors within 3.5 % and 2.7 % for the halogen and fianium sources, respectively. While the theoretical corrections, improve both sources, measurements made with the fianium source produces slightly accurate inverse calculations over the halogen measurements.

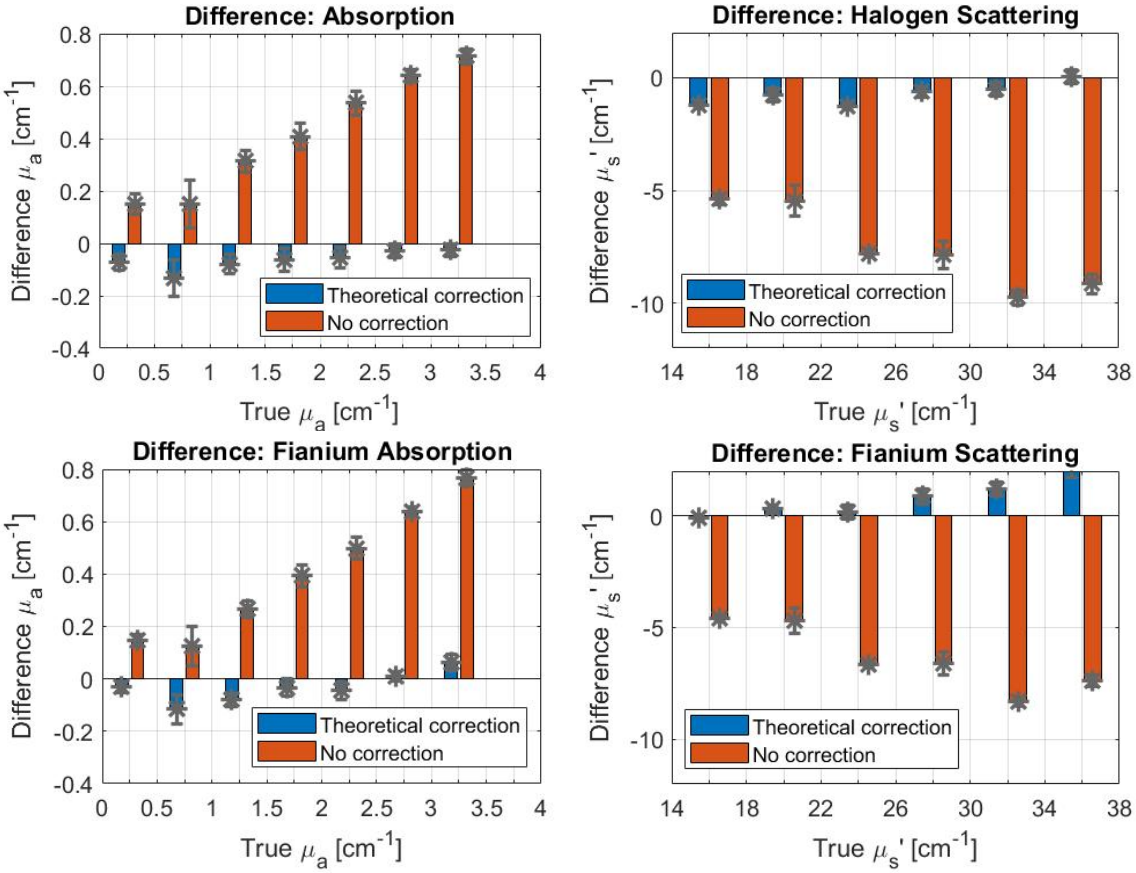

Figure 6.12: comparison of differences in IAD estimated absorption (left) and reduced scattering (right) values against true properties for measurements taken with theoretical correction and no correction. The effects on these differences for both sources - Fianium (below) and Halogen (above) are described.

Incorporation of the theoretical correction has significantly improved the overall resolution of the IS/IAD method to estimate optical properties (Fig. 6.12). For the halogen source, the mean resolution of inverse calculated absorption and reduced scattering have decreased to $0.065\,cm^{-1}$ and $0.74\,cm^{-1}$, respectively. Conversely, for the measurements taken with the fianium source, the resolutions of the system for inverse calculated absorption and reduced scattering have decreased to $0.054\,cm^{-1}$ and $0.81\,cm^{-1}$, respectively. As described above, the incorporation of the experimental correction improves overall resolution of the IS/IAD method to retrieve optical properties

with significant improvement to the inverse calculation over the experimental correction described above.

6.3 Summary of results

I have summarized the performance of the IS/IAD with under varying illumination conditions and correction schemes, as averaged relative errors and resolutions of the system. Here, table 6.1 and 6.2 describes the performance of the system to estimate absorption and reduced scattering. respectively. As observed, for the range of optical properties commensurate with biological tissues, the theoretical correction by the IAD proves to be the best method of estimating optical properties from IS measurements.

Absorption Coefficient (μ_a)	Fianium		Halogen	
	Mean Relative Error (%)	Resolution (cm^{-1})	Mean Relative Error (%)	Resolution (cm^{-1})
No correction	28.02	0.4043	29.37	0.4159
Experimental correction	14.23	0.1849	11.13	0.1722
Theoretical correction	6.42	0.0537	9.65	0.0648

Table 6.1: Table summarizing the results of correction schemes on the ability of the IS/IAD method to estimate absorption coefficients.

Reduced Scattering Coefficient (μ_s')	Fianium		Halogen	
	Mean Relative Error (%)	Resolution (cm^{-1})	Mean Relative Error (%)	Resolution (cm^{-1})
No correction	25.27	6.378	29.89	7.571
Experimental correction	3.26	0.822	8.02	2.012
Theoretical correction	2.7	0.808	3.46	0.739

Table 6.2: Table summarizing the results of correction schemes on the ability of the IS/IAD method to estimate reduced scattering coefficients.

Chapter 7

Conclusions

In this thesis, we have explored the performance of the integrating sphere (IS) and the inverse adding-doubling (IAD) to estimate optical properties of unknown turbid media. Though the IS/IAD method has often been cited as a "gold-standard" method of estimating optical properties, our studies have showed that the IS is prone to inaccurate measurements due to light losses. These inaccuracies commonly lead to errors in IAD calculations. These light losses typically arise due to the geometry of the IS, the source and sample and the losses in power due to the substitution of a sample with a standard. In this thesis, these losses were characterized using a robust stochastic model over a wide range of optical properties. Finally, the two commonly used correction protocols to mediate these losses were investigated providing appropriate guidance to estimate optical with minimal errors.

7.1 Thesis Summary

This section provides a robust summary of this thesis. Chapter 1 introduces the field of tissue optics and the motivation behind optical characterization of turbid media. This optical characterization was done through estimations of quantitative parameters known as optical properties. Finally, this chapter introduces commonly used theoretical models that describe light distribution and propagation across turbid media. Chapter 2, described a method of estimating optical properties using measurements made using an integrating sphere and an appropriate inverse model. Chapter 3 describes the inverse adding-doubling algorithm, that translates IS measurements to optical properties. Here, a detailed account on the benefits of using the IAD over other inverse algorithms is provided. Tests on the accuracy of the model and its sensitivity of various inputs are tested.

The IS/IAD method is then tested using a robust set of optical phantoms that mimic light propagation in tissue-like turbid media. Analysis of these preliminary tests of the system is described in chapter 4. This chapter concludes with a discussion of the possible sources of errors (light losses in IS measurements). Chapter 5 describes a stochastic method of simulating these light losses in

IS measurements for a range of optical properties. These simulations emulate the experimental conditions of a finite sample illuminated by a finite beam, mounted onto an IS port. The results of these simulations indicated that light losses in IS measurement, most significantly affect inverse calculations of low absorption ($< 0.04\,cm^{-1}$) and scattering ($< 3\,cm^{-1}$) samples. Chapter 6 provides a comprehensive analysis of the performance of the IS/IAD method to estimate optical properties under multiple illumination configurations and correction schemes. From our analysis, we observed that measurements made using the Fianium coupled with theoretical correction protocol results in best estimates of absorption and reduced scattering values within resolution of $0.05\,cm^{-1}$ and $0.8\,cm^{-1}$, respectively.

7.2 Future Work

Over the years, various studies to quantify light losses in integrating sphere measurements have been made. As described in this thesis, the performance of the IS/IAD method is highly sensitive to the IS measurements. It must be noted that for the studies conducted here, liquid phantoms are used. Liquid phantoms require the use of glass cuvettes to mount the sample onto the IS port. This leads to mismatches in the boundaries and can lead to inaccuracies in IS measurements. The effect of thick glass cuvettes on IS measurements must be experimentally or theoretically explored.

Appendix A

Input Data files

For the various programs used in this thesis, the optical parameters required by the model for simulations are given in the form of data files. Each data file, corresponding to the algorithm used has a unique structure to its input data files. Here, the structures of these files will be described with examples,

A.1 IAD input file

The basic structure of the input file given to the IAD for inverse calculations, is described below. Important parameters of the sample and sphere along with the inputs of total reflectance and transmittance are required.

```
IAD1   # Must be first four characters

1.33   # Index of sample
1.55   # Index of top and bottom
2.00   # Sample thickness [mm]
2.00   # Thickness of slides [mm]
1.50   # Beam diameter at entrance[mm]
0.99   # Reflectance of calibration standard

1       # Number of spheres used

       # Properties of sphere 1
152.4  # [mm] Diameter of sphere (6 in * 25.4 mm/in)
25.4   # [mm] Sample Port Diameter
25.4   # [mm] Entrance Port Diameter
12.7   # [mm] Detector Port Diameter
```

```
0.99   # Reflectivity of the sphere wall

2   #number of measurements, M_R, M_T
#wavelength     M_R        M_T
500.00       0.095540   0.478146
...
```

A.2 Finite Monte Carlo - Input File

The basic structure of the file describing the tissue structure ("`temp.tissue`") that is later processed by the Finite Monte-Carlo model, is described below. A few of the vital parameters provided in this file are the number of photons simulated, the optical parameters of the sample and the ambient medium. The *xy* dimensions of the sample are specified in the "`mc_globals.h`" file.

```
5000000.00        #number of photons
1                 #number of tissues

##start Tissue 1
1.00              #ref.index top
1.00              #ref.index bottom
1                 # #of layers
#layer 1
0.4839            #mua_x
311.6981          #mus_x
0.0               #mua_m
0.0               #mus_m
0.0               #muaf_x
0.0               #flqy
0.9012            #g_x
0.0               #g_m
0.20              #thickness
1.33              #ref. index
0.0               #TAU
```

Appendix B

MATLAB Code

All the programs described in this thesis, were created in other languages (such as *C*). For streamline the process of simulation and analysis, these programs were run under MATLAB's environment and stored into simple and easily accessible variables. Here, the MATLAB functions implementing the various programs used in this thesis, are described here,

B.1 Adding-Doubling

The MATLAB's invocation of the adding-doubling algorithm to estimate total reflectance and transmittance for a given set of optical parameters pertaining to a sample modelled as a semi-infinite slab, is given here.

```
function [Rt, Tt] = AD_single_io(mua, mus, g, sample_t, n_sample, n_slide)
% The objective of this function is to run the AD for a set of optical
% properties and other sample parameters, under MATLAB's environment.
% Author: Vinoin Devpaul Vincely (created: 2018/06/28)
%
% INPUTS:
%   mua      - absorption coefficient
%   mus      - scattering coefficient
%   g        - anisotropy coefficient
%   sample_t - thickness of sample (in cm)
%   n_sample - refractive index of sample
%   n_index  - refractive index of ambient medium
%
% OUTPUTS:
%   Rt - Total reflection of sample
%   Tt - Total transmission of sample

mut = mua + mus;
```

```
a = mus/mut;          % Albedo
b = sample_t*mut;     % Optical thickness

call = sprintf('ad.exe -m -a %0.8f -b %0.8f -g %0.3f -n %0.3f -s %0.3f ...
    -q 8', a, b, g, n_sample, n_slide);
[~, term_out] = system(call);

vals = strsplit(term_out, ' ');
Rt = str2double(vals{2}); Tt = str2double(vals{4});
```

B.2 Finite Monte Carlo

The implementation of the Finite Monte-Carlo algorithm to operate under MATLAB's environment is described here. Due to the complexity of the process, I have categorized all the relevant sample information into MATLAB "structs". These structures can be obtained by calling the following code ("`vox_MC_inputStrs.m`"),

```
function [sP, gP] = vox_MC_inpStrs(mua, mus, g, nsample, ...
    sample_thickness, xy_dimen, g_mua, g_mus, g_g, nglass, glass_thickness)
% The objective of this function is to creating the input structures ...
    for voc_MC.m (created by: Vinoin Vincely)
%
% INPUTS:
% mua               - sample absorption coefficient
% mus               - sample scattering coefficient
% g                 - sample anisotropy
% nsample           - refractive index of sample
% sample_thickness  - thickness of sample (in cm)
% xy_dimen          - sample xy dimensions
%          (xy_dimen =  [xleft xright yback yfront])
% nglass            - refractive index of the ambient medium
%
% OUTPUTS:
% sP            - structure with optical parameters of sample
% gP            - structure with optical parameters of ambient medium

sP.mua = mua; sP.mus = mus; sP.g = g;
sP.n = nsample; sP.d = sample_thickness;
```

```
20
21 gP.xleft = xy_dimen(1); gP.xright = xy_dimen(2);
22 gP.yback = xy_dimen(3); gP.yfront = xy_dimen(4);
23 gP.n = nglass;
```

With the structures containing the optical parameters describing the to-be modelled tissue, it can be given to the function "`vox_MC.m`". This function writes the new input file (`temp.tissue`) and runs the finite MC program and parses the results out of the generated output file.

```
1  function [params] = vox_MC(sampleProps, glassProps, num_photons, ...
       beam_radius, port_radius)
2  % This function runs the finite MC algorithm under MATLAB's environment.
3  % Run "vox_MC_inpStr" to get input structures.
4  %
5  % INPUTS:
6  % sampleProps   - a structure of sample properties
7  % glassProps    - a structure of glass properties
8  % num_photons   - number of photons for the simulation
9  % beam_radius   - radius of illumination beam (in cm)
10 % port_radius   - radius of collection port (in cm)
11 %
12 % OUTPUT:
13 % param - structure with the following fields
14 %     Rt, Tt, Rt_xleft, Rt_xright, Rt_yfront, Rt_yback
15
16 % ========== Check if vox-MC dump folder exisits ======
17 if ~exist('voxmc_dump', 'dir')
18     fprintf('Making vox-MC dump folder!\n');
19     mkdir('voxmc_dump')
20 end
21
22 cd('voxmc_dump');
23 % ====================================================
24
25 % Current directory
26 my_folder = pwd;
27
28 % Writes the global file
29 cd('~/Documents/LAB/Vox_MC/');
30 vox_MC_global(glassProps.xleft, glassProps.xright, glassProps.yfront, ...
```

```
    glassProps.yback, glassProps.n, glassProps.n, glassProps.n, ...
    glassProps.n, beam_radius, port_radius);

% Run "make" file to get executable
[¬,¬] = system('make clean'); [¬,¬] = system('make time');
copyfile('vox_mc', my_folder, 'f');
cd(my_folder);

% Write the tissue file
vox_MC_tissue(sampleProps.mua, sampleProps.mus, sampleProps.g, ...
    sampleProps.n, sampleProps.d, glassProps.n, num_photons);

% Lets run VOXEL-MC
system('./vox_mc temp.tissue');

% To parse out MC dumps
dumps = vox_MC_logTR_parser('TR_dump.log');
params.dump = dumps(end);
[params.Rtcol, params.Ttcol] = ...
    vox_MC_RTrho_parser(char(strcat('RTrho_', params.dump)), num_photons);
[params.Rt, params.Tt, params.Rt_xleft, params.Rt_xright, ...
    params.Rt_yfront, params.Rt_yback] = ...
    vox_MC_dump_parser(char(params.dump), num_photons);
params.Rsp = ((glassProps.n-sampleProps.n)/(glassProps.n+sampleProps.n))^2;

cd ..;
```

The output of this function is a structure (”`params`”) containing the fluences corresponding to the surface of exit of the modelled tissue.

References

[1] Steven L. Jacques. Optical properties of biological tissues: a review. *Physics in Medicine and Biology*, 58:R37–R61, 2013.

[2] Wai-Fung Cheong, Scott A. Prahl, and Ashley J. Welch. A review of the optical properties of biological tissues. *IEEE Journal of Quantum Electronics*, 26:2166–2185, 1990.

[3] Rebecca Richards-Kortum and Eva M. Sevick-Muraca. Quantitative optical spectroscopy for tissue diagnosis. *Annual Review of Physical Chemistry*, 47.

[4] Willem M. Star. *Diffusion Theory of Light Transport*, pages 131–206. Springer US, Boston, MA, 1995.

[5] Lihong Wang, Steven L. Jacques, and Liqiong Zheng. Mcml - monte carlo modeling of light transport in multi-layered tissues. *Computer Methods and Programs in Biomedicine*, 47(2):131–146, 1995.

[6] TJ Farrell, MS Patterson, and B Wilson. A diffusion-theory model of spatially resolved, steady-state diffuse reflectance for the noninvasive determination of tissue optical-properties invivo. *Medical Physics*, 19(4):879–888, Jul-Aug 1992.

[7] Michael S. Patterson, B. Chance, and B. C. Wilson. Determining the optical properties of turbid media by using the adding-doubling method. *Applied Optics*, 32(4):559–568, 1993.

[8] Alexey N. Bashkatov, Elina A. Genina, and Valery V. Tuchin. Optical properties of skin, subcutaneous, and muscle tissues: a review. *Journal of Innovative Optical Health Sciences*, 4:9–38, 2011.

[9] L Mosegaard and A Tarantola. Monte-carlo sampling of solutions to inverse problems. *Journal of Geophysical Research-Solid Earth*, 100(B7):12431–12447, 1995.

[10] John W. Pickering, Niek van Wieringen S.A.P., Johan F. Beek, Henricus J. C. M. Sterenborg, and Martin J. C. van Gemert. Double-integrating-sphere system for measuring the optical properties of tissue. *Applied Optics*, 34:399–410, 1993.

[11] Lihong V. Wang and Hsin-I Wu. Summary of mie theory.

[12] S. L. Jacques, C. A. Alter, and S. A. Prahl. Angular dependence of hene laser light scattering by human dermis. *Lasers in the Life Sciences*, 1(4):309–334, 1987.

[13] Scott A. Prahl. The adding-doubling method. In H. Kogelnik, editor, *Optical-Thermal Response of Laser-Irradiated Tissue*, chapter 5, pages 101–128. Plenum publishing co., 233 Spring St., New York, New York, 1995.

[14] H.C. [VAN DE HULST], editor. *Front Matter*, page iii. Academic Press, 1980.

[15] J. Quincy Brown, Karthik Vishwanath, Gregory M. Palmer, and Nirmala Ramanujam. Advances in quantitative uv-visible spectroscopy for clinical and pre-clinical application in cancer. *Current Opinion in Biotechnology*, 20(1):119–131, 2009.

[16] E. Teran-Bobadilla, E.R. Mendez-Mendez, R. Quispe-Siccha, A. Perez-Pacheco, and F.L.S. Cuppo. Application of single integrating sphere system to obtain the optical properties of turbid media. *OSA Continuum*, 2(5), 2019.

[17] *Integrating Sphere Theory and Applications*.

[18] I. V. Yaroslavsky, A. N. Yaroslavsky, T. Goldbach, and H.-J. Schwarzmaier. Inverse hybrid technique for determining the optical properties of turbid media from integrating-sphere measurements. *Applied Optics*, 35(34), 1996.

[19] Brian C. Wilson. Measurement of tissue optical properties: Methods and theories. In Ashley J. Welch and Martin J.C. van Gemert, editors, *Optical-Thermal Response of Laser-Irradiated Tissue*, chapter 8, pages 233–274. Plenum publishing co., 233 Spring St., New York, New York, 1995.

[20] Shu Zhang, Xiaohua Wu, Shushui Zhang, Qiluan Cheng, and Zuojun Tan. An effective method to inspect and classify the bruising degree of apples based on the optical properties. *Postharvest Biology and Technology*, 127.

[21] Tamara L. Troy. Optical properties of human skin in the near infrared wavelength range of 1000 to 2200 nm. *Journal of Biomedical Optics*, 6:167–176, 2001.

[22] Wouter Saeys, Maria A. Velazco-Roa, Suresh N. Thennadil, Herman Ramon, and Bart M. Nicolai. Optical properties of apple skin and flesh in the wavelength range from 350 to 2200 nm. *Applied Optics*, 47:908–919, 2008.

[23] Gregory M. Palmer and Nirmala Ramanujam. Monte carlo-based inverse model for calculating tissue optical properties. part i: Theory and validation on synthetic phantoms. *Applied Optics*, 45(5):1062–1071, 2006.

[24] Elena Salomatina, Brian Jiang, John Novak, and Anna N. Yaroslavsky.

[25] Grant I. P. and Hunt G. E. Discrete theory of radiative transfer .1: Fundamental. *Proceedings of the Royal Society London A*, 313, 1969.

[26] S.A. Prahl. *Light Transport in Tissue*. PhD thesis, The University of Texas at Austin, 1988.

[27] J.A. Nelder and R. Mead. A simplex-method for function minimization. *COMPUTER JOURNAL*, 7(4):308–313, 1965.

[28] Ben Aernouts, Eduardo Zamora-Rojas, Robbe Van Beers, Rodrigo Watté, Ling Wang, Mizuki Tsuta, Jeroen Lammertyn, and Wouter Saeys. Supercontinuum laser based optical characterization of *Intralipid*® phantoms in the 500-2250 nm range. *OPTICS EXPRESS*, 21(26), 2013.

[29] PK Jain, KS Lee, IH El-Sayed, and MA El-Sayed. Calculated absorption and scattering properties of gold nanoparticles of different size, shape, and composition: Applications in biological imaging and biomedicine. *Journal of Physical Chemistry B*, 110(14):7238–7248, 2006.

[30] H. Buiteveld, J. M. H. Hakvoort, and M. Donze. The optical properties of pure water. *SPIE Proceedings on Ocean Optics XII*, 2258, 1994.

[31] P Nostell, A Roos, and D Ronnow. Single-beam integrating sphere spectrophotometer for reflectance and transmittance measurements versus angle of incidence in the solar wavelength range on diffuse and specular samples. *REVIEW OF SCIENTIFIC INSTRUMENTS*, 70(5):2481–2494, MAY 1999.

[32] Scott Prahl. *Everything I think you should know about Inverse Adding-Doubling*. Oregon Medical Laser Center.

[33] Jisoo Hwang, Dong-Joo Shin, and Ki Ryong Jeong. Integrating sphere-based relative methods for reflection measurements. *METROLOGIA*, 53(6), DEC 2016.

[34] Holly L. Gorton, Craig R. Brodersen, William E. Williams, and Thomas C. Vogelmann. Measurement of the Optical Properties of Leaves Under Diffuse Light. *PHOTOCHEMISTRY AND PHOTOBIOLOGY*, 86(5):1076–1083, SEP-OCT 2010.

[35] Steven L. Jacques and Lihong Wang. Monte carlo modeling of light transport in tissues. In Ashley J. Welch and Martin J.C. van Gemert, editors, *Optical-Thermal Response of Laser-Irradiated Tissue*, chapter 4.1-4.7, pages 73–99. Plenum publishing co., 233 Spring St., New York, New York, 1995.

[36] K Vishwanath, B Pogue, and MA Mycek. Quantitative fluorescence lifetime spectroscopy in turbid media: comparison of theoretical, experimental and computational methods. *Physics in Medicine and Biology*, 47(18):3387–3405, 2002.

[37] Luka Vidovic and Boris Majaron. Elimination of single-beam substitution error in diffuse reflectance measurements using an integrating sphere. *JOURNAL OF BIOMEDICAL OPTICS*, 19(2), FEB 2014.